Dehydrogenation of Liquid Organic Hydrogen Carriers on Model Catalyst Surfaces

Dehydrierung von flüssigen organischen Wasserstoffspeichern auf Modellkatalysatoroberflächen

Der Naturwissenschaftlichen Fakultät

der Friedrich-Alexander-Universität Erlangen-Nürnberg

zur

Erlangung des Doktorgrades Dr. rer. nat.

vorgelegt von

Christoph Gleichweit

aus Graz

Als Dissertation genehmigt
von der Naturwissenschaftlichen Fakultät
der Universität Erlangen-Nürnberg

Tag der mündlichen Prüfung: 29.10.2015

Vorsitzender des Promotionsorgans: Prof. Dr. Jörn Wilms
Gutachter: Prof. Dr. Hans-Peter Steinrück
Prof. Dr. Jörg Libuda

Contents

1 Introduction

Today's energy supply is dominated by carbon-based fossil fuels. Eighty seven percent of the world-wide primary energy demand was satisfied by oil, coal and gas in 2013.[1] They offer some advantages, such as being easily accessible and exhibiting a high storage density[2], but depletion of these natural resources is not sustainable and leads to anthropogenically-induced climate change due to the resulting CO_2 emissions.[3] The route away from rapid depletion of natural resources is using renewable energy sources such as wind and solar energy. But these renewable sources involve fluctuations in energy output time- and location-wise, caused by their dependence on weather conditions. For a steady energy supply this creates the need for efficient distribution and storage systems.[4] Presently, suitable concepts to overcome the distribution problem involve extension of the electric grids, while storage remains as the major challenge to face. Electrical energy storage nowadays is performed nearly exclusively (99%) by pumped hydroelectric systems, while other technologies such as compressed air and battery grid storage only play a minor role.[5, 6] Thus, there is great interest in developing alternative concepts for both storage and distribution of energy.

Among the compounds suitable for energy storage, hydrogen has the highest gravimetric storage density (33 kWh kg^{-1}). Unfortunately, present physical hydrogen storage methods exhibit apparent drawbacks.[7] To avoid high pressures (up to 700 bar) needed for compressed storage in the gaseous state or the cryogenic temperatures (-253°C) in the liquid state, chemical storage methods are needed. Among these methods, e.g. metal hydride materials[8], and reactions with alcohols are studied.[9-11] However, research has to be done on all of these methods to overcome persisting issues, and in the long term, to bring them to market maturity. In the following, a novel approach of chemical hydrogen storage is introduced.

1.1 Liquid Organic Hydrogen Carriers

The idea of storing hydrogen in liquid organic compounds has been discussed recently.[2, 12-17] The concept of energy storage and distribution in so-called liquid organic hydrogen carriers (LOHCs) is described in the following: first the molecules are loaded with hydrogen to form the energy-rich state at a facility with access to hydrogen (e.g. from electrolysis) by catalytic hydrogenation. This is followed by distribution to a place which is in need of energy, where the unloading is performed, that, is the release of the stored hydrogen from the molecule as gas; the gas is then available for consumption, e.g. in a fuel cell. The resulting energy-lean form of the compound is

then transported back to the facility, closing the cycle of both energy storage and distribution (see Fig. 1.1). This way, the carrier compound travels back and forth from the source of energy to the place of use. LOHCs mostly consist of aromatic/alicyclic organic hydrocarbons, exhibiting physico-chemical properties close to diesel, which ensures operability in established infrastructure build for fuel distribution.[2]

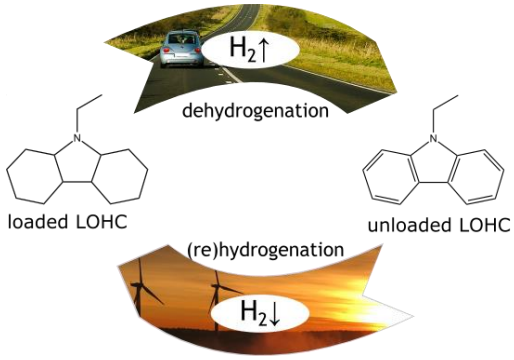

Fig. 1.1: Sketch of the concept of using LOHCs in energy storage applications

Both loading and unloading are performed by catalyzed chemical reactions. To provide for an efficient LOHC storage system, both the carrier molecule and the catalysts used for the loading/unloading cycles have to be optimized. For a carrier molecule, properties such as storage density, liquid range, toxicity, thermal stability and large-scale availability have to be considered.[18] Concerning the catalyst, balancing price and efficiency is important to establish a competitive storage technology.[19]

1.2 Surface science approach to catalysis

In the field of chemistry, catalysis plays an important role. According to the IUPAC definition, catalysis is the action of a catalyst, which is "a substance that increases the rate of a reaction without modifying the overall standard Gibbs energy change in the reaction".[20] Catalysts thus are not consumed in reactions.

If the catalyst is present in a different phase than the other reactants, the term heterogeneous catalysis is used. An important prototypical reaction for LOHCs is the hydrogenation, that is, loading of unsaturated hydrocarbons using metal catalysts. For example, the hydrogenation of ethylene to produce ethane is performed typically over platinum or nickel:[21]

$$H_2C = CH_2 + H_2 \xrightarrow{\text{Catalyst}} H_3C - CH_3$$

The process involves the steps of adsorption and dissociation of H_2 on the metal to form adsorbed hydrogen (H_a), and also the adsorption of ethylene ($C_2H_{4,a}$). Adsorbed hydrogen atoms react with the double bond of ethylene to form adsorbed ethane ($C_2H_{6,a}$). Desorption of the product from the metal surface completes the process.

All these steps prove essential for the reaction to occur.[21] Thus understanding the details is of great interest to optimize the reaction. The field of surface chemistry aims at a fundamental understanding of the microscopic processes of reactions at solid/liquid or solid/gas interfaces, such as adsorption, desorption, diffusion, dissociation and reaction. To investigate these individual processes separately, the studied system must be simplified and experimental techniques are needed that probe the surface processes. The techniques commonly applied to gain information on these fundamental processes involve spectroscopic and microscopic methods that probe flat solid catalyst surfaces, which are usually low indexed facets of metal single crystals.[22] A drawback arises from the so-called "material gap". Using a single crystal facet as a model system for a real catalyst simplifies the system. But the complexity of the catalyst materials used in industry is usually much higher, as they typically consist of small particles on a support. These particles exhibit a number of different facets and usually defects like steps and kinks on the surface. Metal atoms at these defect sites show higher reactivity due their lower coordination, and therefore play an important role.[22] Nonetheless, predictions made from studies on single crystals give fundamental insights in the catalytic processes involved under industrial conditions, which may help improving and understanding reactions in real catalysis, and might pave the way towards knowledge driven catalyst design.[23]

Surface science experiments were performed to study the chemical reactions of LOHC molecules on metal single crystals using surface-sensitive spectroscopic methods. Most of these experimental techniques rely on electron detection and therefore require ultra-high vacuum (UHV) conditions (pressures lower than 10^{-7} mbar) to operate electron energy analyzers. Another reason for working under these conditions is to provide for a highly defined environment during the experiments, since any disturbing influence of unwanted residual gases is suppressed. A drawback of performing experiments in UHV is the so-called "pressure gap", that is, the difference of pressure between the experimental (UHV) and the reaction conditions (usually ambient pressures or higher).[22] Noteworthy, there are some novel experimental setups for photoelectron spectroscopy which are able to bridge the pressure gap under in-situ conditions.[24, 25] However, these methods are not used in this work.

Pt-group metals (Ru, Rh, Os, Pd, Ir, Pt) exhibit a high catalytic reactivity due to their partially filled d-bands crossing the Fermi level.[26, 27] Pt in particular shows such crossing d-bands[28] (configuration: [Xe] $4f^{14}$ $5d^{9}$ $6s^{1}$) and is commonly used in heterogeneous catalysis in a variety of important applications.[29] It is the active substance in catalytic converters of cars[30], and will become more and more important for arising applications such as fuel cell electrocatalysts.[31] In chemical industry, it is used for hydrocarbon reforming processes, hydrocarbon cracking reactions, hydrogenation of liquid vegetable oil etc.[30] Platinum shows also pronounced activity for dehydrogenation reactions of saturated hydrocarbons such as LOHCs.[2, 15] In this thesis, UHV studies have been performed on LOHC dehydrogenation reactions that are limited to the (111) facets of Pt and Pd as model catalysts (see Chapter 4). This continues the preliminary work[32] on LOHCs that has already been conducted in our group.

However, Pt-group metals exhibit an apparent drawback: their rare abundance[30] at the currently high demand on the market leads to high prices. As availability studies reveal even a worsening of the situation, the need for alternative catalyst materials arises[33], especially if one wants to realize the idea of storing hydrogen in LOHCs. Early transition metal carbides (TMCs) have attracted attention due to their similar catalytic behavior as the Pt-group metals[34] and their comparably low prices.[35] In addition to the studies on LOHCs, fundamental investigations on carbide-modified surfaces as model catalysts have been performed in this thesis (see Chapter 5).

This dissertation is a cumulative thesis, which is based on seven publications with exclusive or major contributions from the author (six have already appeared and one is close to submission). The work was performed in collaboration with the groups of Prof. Jörg Libuda and Prof. Andreas Görling in Erlangen. In the next chapters, an overview of the applied techniques and the experimental setups is given, followed by an extended summary of the achieved results: In Chapter 2, a short description of the fundamentals and techniques is presented, providing the reader with the theoretical background for a better understanding of the results presented in Chapter 4 and 5. Furthermore, in Chapter 3 the experimental setups are described that were used for the measurements. In Chapter 6 the thesis is summarized in English, and is followed by a German “Zusammenfassung” in Chapter 7. Finally, the appendix contains the publications P1 - P7.

2 Fundamentals and techniques

2.1 Synchrotron-based radiation

Synchrotrons are particle accelerators, in which charged particles (electrons or ions) are accelerated to high (relativistic) speed.[36] To give a charged particle a curved motion it needs to be deflected, which is typically done by a number of bending magnets. The deflection leads to emission of electromagnetic radiation with an energy loss per cycle of[37]

$$\Delta E = \frac{(Ze)^2 E^4}{3\varepsilon_0 R\,(m_0 c^2)^4} \tag{1}$$

with Z being the particle's charge number, e the elementary charge, ε_0 the electrical field constant, E the particle energy, R the curvature radius, m_0 the particle's reduced mass and c the speed of light. The dependence on the 4th power of the kinetic energy E of this relation shows that the emitted energy grows dramatically when the velocity approaches the speed of light. Moreover, because of the mass dependence, the particles with the lowest mass emit the most radiation. Therefore electrons are commonly used if a maximum yield of radiation is intended.

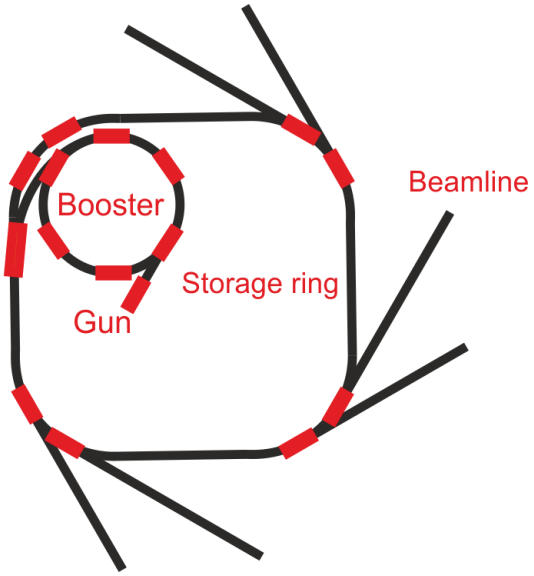

Fig. 2.1: *Sketch of a synchrotron light source. An electron gun injects electrons into the booster synchrotron, which accelerates the electrons to the final energy used in the storage ring.*

Synchrotron radiation covers a wide range of the electromagnetic spectrum. The amount of radiation, i.e., the photon flux, of synchrotrons exceeds the one from conventional lab sources by

orders of magnitude. Further important properties of the radiation emitted at synchrotrons are the tunable X-ray energy, the high brilliance and the tunable polarization.[38]

Nowadays, synchrotron light sources, a special type of these synchrotron facilities, are realized as large-scale scientific institutions.[36] They are constructed to serve as a light source for experiments that require electromagnetic radiation. State-of-the-art facilities consist of a storage ring, which is used for the generation of radiation. The acceleration and injection of electrons into these storage rings is usually done by additional, smaller apparatuses that accelerate the electrons to the desired energy (electron guns and booster synchrotrons, see Fig. 2.1).

2.2 X-ray photoelectron spectroscopy (XPS)

Photoelectron emission is the phenomenon that electrons are emitted from a material when light shines on it. It is caused by the photoelectric effect, first proposed by A. Einstein[39] in 1905, and is a subsequent mechanism to the absorption of light by matter.[40]

Upon irradiation of a conducting sample by electromagnetic radiation, energy conservation yields

$$E_{kin} = h\nu - E_B - \phi \tag{2}$$

with E_{kin} being the photoelectron kinetic energy, E_B the binding energy of the electron and ϕ the work function of the sample.

Photoelectron spectroscopy (PES) is the technique of determining the kinetic energy of these emitted photoelectrons. In experimental setups, the kinetic energy is measured using electron energy analyzers. As the work function of solid surfaces is not generally known, the Fermi energy E_F is commonly used as a reference for both the kinetic energy E_{kin} and the binding energy E_B. For this reason, the detector and the sample are set to the same electric potential by linking them electrically. Considering the work function of the analyzer ϕ_A, the above equation changes to[36]

$$E_{kin} = h\nu - E_B - \phi_A \tag{3}$$

Depending on the used excitation energy, electrons can be emitted from mainly the valence states ($h\nu$ < 100 eV, ultraviolet photoelectron spectroscopy, UPS), or also from the electron core levels ($h\nu$ > 100 eV), for which the term X-ray photoelectron spectroscopy (XPS) is used. Fig. 2.2 depicts the different energy regimes of XPS and UPS in a schematic drawing of the electron states in a solid material.

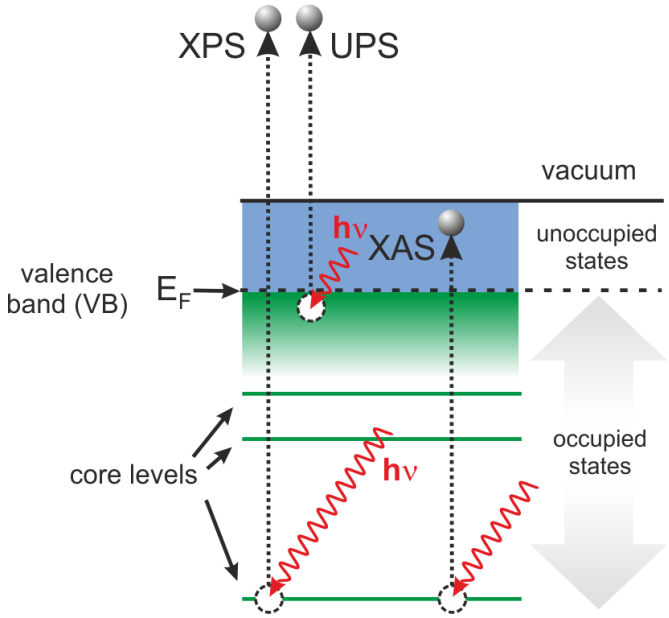

Fig. 2.2: *Schematic sketch of photoelectron spectroscopy and absorption spectroscopy. In XPS and UPS the electrons are emitted into the vacuum from valence or core level states, whereas in XAS core-level electrons are excited to unoccupied states in the valence band*

XPS is a widespread analytical method to study the physics and chemistry of surfaces.[41-43] The surface sensitivity is due to the low elastic mean free path of electrons (5 – 30 Å) in the energy range XPS is typically conducted. In Fig. 2.3a, the example of an XP spectrum of Pt(111) is shown. For traditional reasons, the binding energy axis is always displayed in reverse, since this way the kinetic energy increases to the right. The difference between incident photon energy and binding energy of the electrons (see Eq. 3) leads to the peaks at the kinetic energy axis of a spectrum (see Fig. 2.3b). Because the core level energies of different chemical elements differ strongly, the positions of the peaks are specific to the chemical elements. Note that in the example displayed in Fig. 2.3, besides platinum (Pt) also impurities such as calcium (Ca), carbon (C) and oxygen (O) are detected. Using the information on the elemental constituents, the chemical composition of a sample surface can be determined.

Additionally, the binding energy E_B measured using XPS is influenced by the valence electron density at the core electrons. The interaction of an X-ray photon with a core electron leads to a change in its state: the electron changes from the initially bound state in the core orbital of the atom to a final, unbound state. Both initial and final state effects influence the measured binding energy. Possible final state effects include a shift of the energy that occurs when the removal of one electron leads to a lowering of the overall system energy by relaxation of the remaining

electrons, and to other effects such as excitation of further electrons into unoccupied bound valence band states (shake up) or unbound states (shake off).[40, 44]

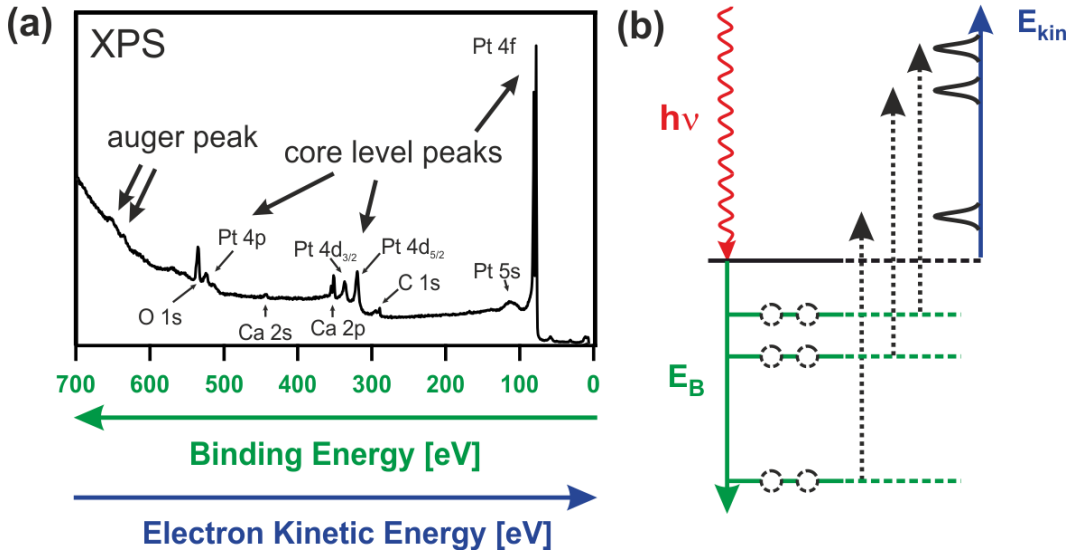

Fig. 2.3: *(a) Example of an XP spectrum of Pt(111), containing core level and Auger peaks. (b) Schematics describing the origin of the individual core hole peaks in an XP spectrum.*

A superposition of final state and initial state contributions leads to the so-called chemical shift. This effect provides additional information on the chemical bonds in the system[36, 40], and makes XPS a powerful method to also study chemical reactions on surfaces. Energetic shifts up to the order of a few electronvolts (eV) can be observed between different oxidation states of metals (e.g. Mo).[45] Another example of the chemical shift is the surface core level shift (SCLS). It is (mostly) an initial state effect that is due to the lower coordination of surface atoms of a solid.[46] The resulting binding energy differences (below 1 eV) may be only detected using setups that have a sufficient energy resolution. Both incident beam spectral line width and analyzer resolution have to be sufficient to detect the shifts.

During the photoemission process, the outgoing electron may interact with the surrounding matter. Examples of such inelastic scattering effects are electronic excitations (e.g. excitation of electron-hole pairs in metals), and vibrational excitations. If the primary electron experiences multiple energy loss events, its kinetic energy is decreased even further. These effects lead to the steep increase of XPS spectra at low electron kinetic energies (see Fig. 2.3a).

In principle, the area of an XPS peak is proportional to the abundance of the respective element as the photoemission cross section is independent from the chemical surrounding; thus XPS is a quantitative method. However, one effect that one has to keep in mind is photoelectron diffraction (PED), which might influence the intensity of XPS peaks. This phenomenon, induced by

interference of the primary photoelectron wave with scattered electron waves, leads to intensity differences as a function of emission angle and photoelectron kinetic energy. It is observed particular at low kinetic energy of the electrons (~100 eV).[47]

In this work, isothermal adsorption experiments of molecules on surfaces have been monitored using XPS, and heating experiments denoted as temperature-programmed XPS (TPXPS) have been conducted. For a more detailed discussion that deals with the treatment of the background of XPS spectra and with the quantitative analysis including peak fitting in this work, see the PhD thesis of M. Kinne.[48]

2.3 Near-edge X-ray absorption fine structure (NEXAFS)

In X-ray absorption spectroscopy (XAS), the change of the system as a function of excitation energy is monitored. In contrast to photoemission studies, the photon energy is scanned, rather than the energy of the emitted electrons. The amount of light absorbed in a material is proportional to the absorption coefficient μ. It shows strong dependence both on the atomic number Z and the photon energy $h\nu$:

$$\mu \sim \frac{Z^4}{E^3} \tag{4}$$

The intensity loss by absorption of X-rays in a sample of thickness d is described by Beer's Law for linear absorption[36]

$$I = I_0 e^{-\mu d} \tag{5}$$

where I_0 is the incident intensity and I is the transmitted intensity.

Moreover, properties of the material such as the atom density distribution, the type of bond, magnetic properties and the polarization of the X-rays show an influence on the absorption behavior. Consequently, XA spectra exhibit a variety of characteristic features. As indicated in Fig. 2.2, excitations from a core-electron to an unfilled valence state are possible processes. Important for absorption studies is the relaxation of these excited states, which may happen via emission of photons, photoelectrons or Auger electrons.

The discussion here will be limited to core-level absorption edges, since they prove to be quite valuable in the analysis of molecules adsorbed on surfaces. The *K*-edge originates from the absorption due to a resonance of the excitation energy with the ionization threshold (I.T.) of the

1*s* state (*K*-shell). Strong fluctuations are found near the edge, since this region is dominated by excitation of electrons from the core-level to unoccupied (bound) valence states and also to the quasi-continuum right above the I.T.[36, 49]

This region is commonly referred to as near-edge X-ray absorption fine structure (NEXAFS) or X-ray absorption near-edge structure (XANES). It contains information about the electronic structure of the material, due to the transition of electrons to unoccupied orbitals. Due to the complexity of the process, these spectra have been mostly interpreted qualitatively in the past rather than being quantitatively analyzed.[36] However, the fact that NEXAFS probes the unoccupied states makes it complementary to photoemission techniques, since these probe occupied states.

Organic compounds are widely studied using NEXAFS.[49] Similar to the case of solids, three energy regimes are found for electrons in a molecule: the region of occupied (bound) states, of unoccupied (bound) states and free movement above the I.T. (see. Fig. 2.4). In the pre-edge region of an XA spectrum, the energy is still too low to excite an electron to the vacuum, but it is already sufficient to induce a transition to unoccupied bound states (below the I.T.) such as the lowest unoccupied molecular orbital (LUMO). A NEXAFS spectrum of graphene on Pt(111) is shown in Fig. 2.4. Near the *K*-edge (C 1*s*) the absorbed intensity shows a sharp resonance, which is due to an excitation to the unoccupied π^* orbitals of graphene. Above the I.T., one finds mostly transitions to quasi-bound σ^* orbitals.[49-51]

The intensity of the resonances of the individual orbitals depends both on the density of states at that energy and the selection rules. The isolated nature of the molecular states leads to quite strict selection rules that govern the transition from a core-level to an unoccupied state. The orientation of the X-ray electric field (the polarization of the incident light) relative to the polarization direction of the orbitals has a great influence on the absorption probability. This way, the orientation of molecular orbitals can be probed by changing the incident light polarization in between the measurements.[49]

NEXAFS spectra can be acquired in either electron- or fluorescence yield mode. The X-ray absorption process leads to a core hole and either an excited electron around the I.T. or a photoelectron well above the I.T. Subsequently the core-hole is filled by an electron accompanied either by emission of a photon (fluorescence) or by the emission of an Auger electron. Therefore, collecting the electrons (photoelectrons, Auger electrons and secondary electrons) and the emitted photons are both a measure for the absorption cross section. However, the channels do not show

the same yield. Electron yield detection shows a higher surface sensitivity due to the low electron mean free path in matter (see chapter on XPS).[38]

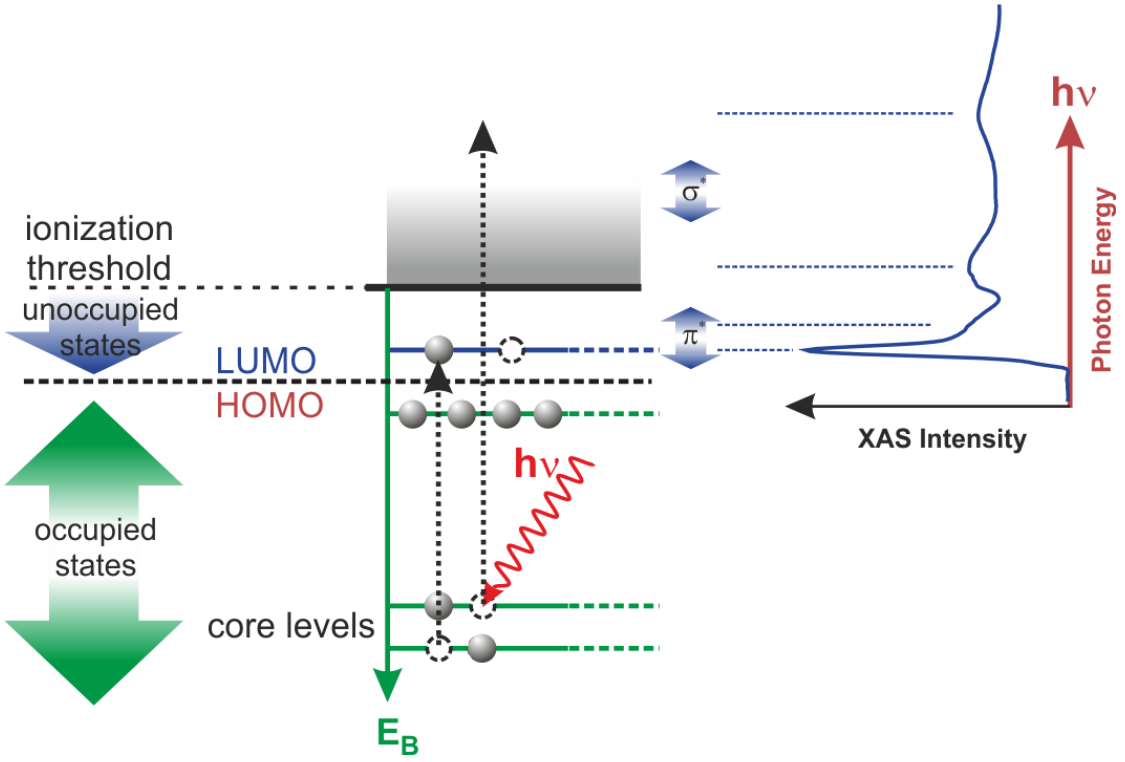

Fig. 2.4: *A NEXAFS spectrum typically consists of sharp resonances originating from the unoccupied bound states below the ionization threshold (I.T.) and broader features above the I.T. The example spectrum on the right shows a spectrum of graphene, an unsaturated organic compound. The lowest unoccupied orbitals (LUMO) are π* orbitals, and σ* orbitals are found above the IT.*

2.4 Temperature-programmed desorption (TPD)

A complementary method to study surface reactions by monitoring the surface (XPS and NEXAFS) is to monitor the gas phase during a heating experiment. Temperature-programmed desorption (TPD) is a widespread and powerful tool to investigate the desorption of gases from solids. In a typical TPD experiment, a solid (e.g. a single crystal) is heated with a linear temperature ramp at a rate β, leading to thermally induced desorption from the surface, while the gas-phase is monitored using a quadrupole mass spectrometer (QMS).[22, 52] Under the assumption that readsorption can be ignored (pumping speed is infinitely high), the desorption rate from a surface is given by the Polanyi-Wigner equation:[53]

$$r = -\frac{\partial\theta}{\partial t} = \nu_i \theta^i e^{-E/RT} \tag{6}$$

where θ is the surface coverage, ν_i is the preexponential factor for a process of order i, E is the desorption activation energy, T is the surface temperature and R is the ideal gas constant.

Desorption of atoms or molecules from surfaces follows different kinetics dependent on how the process happens. First-order kinetics ($i = 1$) occur if single atoms desorb (non-associatively); then the rate of desorption decreases together with the coverage. Some molecules (e.g. H_2 on Pt(111)) adsorb dissociatively by cracking, and also desorb associatively. Thus the atoms have to "find" each other on the surface prior to the desorption event. Second-order ($i = 2$) kinetics is expected, if recombination precedes desorption (e.g. $H + H \rightarrow H_2$). Also zero-order desorption ($i = 0$) is observed for particular systems such as multilayers of molecules on surfaces.

There is a number of methods to analyze the TPD spectra both qualitatively and quantitatively.[22, 54] Using the "leading edge analysis", desorption energy and preexponential may be extracted from the low temperature onset of the TPD spectra.[55] However, to avoid significant errors in the analysis, a large amount of high quality data is needed. For a rough guess of the desorption parameters, the Redhead analysis[56] is widely used. As a rule of thumb, the relation of the peak temperature to the activation energy for first-order desorption is

$$E = RT_p(\ln(T_p\nu_1/\beta) - 3.46) \tag{7}$$

where T_p is the desorption peak maximum temperature and the preexponential factor ν_1 is usually guessed. When using this equation, the peaks have to be well resolved, and lateral interactions need to be minor.[22]

3 Experimental setup

3.1 Synchrotron UHV setup

The XPS and NEXAFS measurements were conducted at the synchrotron facility BESSY II at beamline U 49/2 PGM 1 using a custom-made transportable UHV apparatus[48, 57]; a picture of it is found in Fig. 3.1. It consists of a preparation chamber, an analysis chamber and a supersonic molecular beam chamber. The preparation chamber consists of a sputter gun, a LEED optics, electron beam evaporators and dosing facilities. The analysis chamber houses the connection to the beamline and a hemispherical electron analyzer (Omicron EA 125 HR U7), a dosing facility for LOHCs and a quadrupole mass spectrometer (Pfeiffer Vacuum Prisma QME200).

Fig. 3.1: *Picture of the "synchrotron machine"*

A supersonic molecular beam is also directly attached to the analysis chamber, allowing for high local pressures at the sample (up to 10^{-5} mbar), while the background pressure of the chamber is about three orders of magnitude lower. It consists of three differentially pumped stages. The first one contains the nozzle, and a skimmer that allows only gas from the zone of silence to reach the second stage.[58] In the second stage, a pneumatic shutter is installed as a fast switch. Apertures between the second and third stage spatially confine the beam to fit the size of the sample. Additionally, a beam monitor is installed at the opposite side of the analysis chamber for beam calibration.

A manipulator in the preparation chamber allows for translation of the sample in all three spatial directions as well as rotation around two rotational axes, and to move the sample into the analyzer chamber. Liquid nitrogen allows cooling down to approximately 110 K, and by resistive heating temperatures up to 1300 K may be reached. In addition, a filament at the back of the sample enables XPS measurements while heating up to about 600 K.

3.2 NEXAFS Detector Setup

For the NEXAFS measurements, a setup for partial electron yield (PEY) measurements (see Chapter 2.3) was built in this thesis. It consists of the in-vacuum part (channeltron Photonis CEM 4716 TRI and a retardation grid) and of the electronics that are connected to it. This setup can be easily attached to the analysis chamber of the synchrotron UHV setup (see previous chapter) or to any other UHV machine.

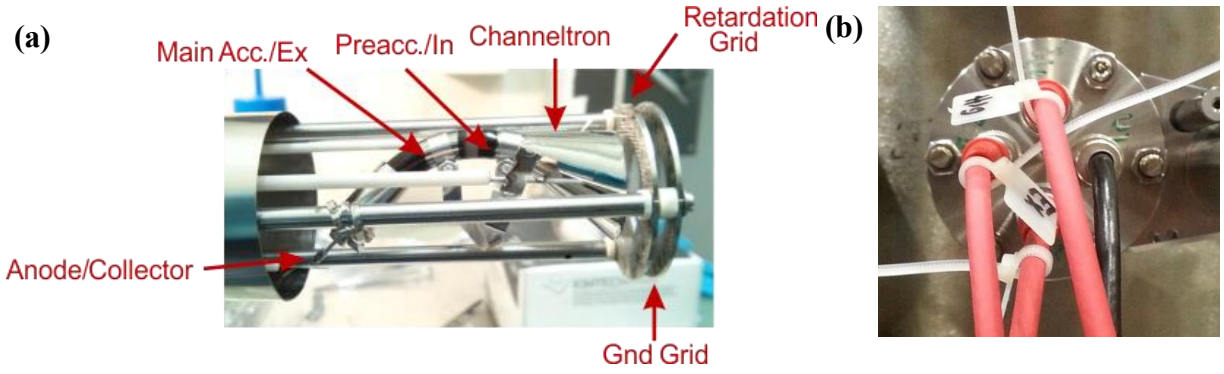

Fig. 3.2: *(a) UHV picture of the partial electron yield detector; (b) high-voltage feed-through from the outside. A description is found in the text.*

In Fig. 3.2a the PEY detector, including the channeltron, is shown. There are four connectors that need to be wired correctly (see Fig. 3.2b). The first grid (from the right) acts as shielding to keep the space in front of the detector free of any electric fields. Next, there is the repulsion grid. For PEY detection, it is set to a negative voltage; for total electron yield (TEY) this grid is connected to ground. The pre-accelerating voltage collects all electrons that passed the repulsion grid, and the main accelerating voltage causes the signal gain. At the collector (anode) the measurement signal is obtained. Note that the detector can also be used to operate in positive ion detection mode. See Appendix B for a detailed wiring diagram of the channeltron and the grids and for technical data.

The measurements are performed by varying the photon energy while the output signal (anode) is monitored (see Chapter 2.3). Beamline U 49/2 PGM 1 at BESSY II provides X-ray radiation at

a photon energy range of ~100-1000 eV that is linearly polarized with an orientation of the E-field vector in-plane with the storage ring (parallel to the floor). The so-called “continuous mode" allows for simultaneous movement of undulator and monochromator at specified speeds, providing for smooth measurement signals during photon energy ramps. An example of a spectrum (graphene on Pt(111)) obtained with this setup is displayed in Fig. 2.4.

3.3 TPD UHV setup

The TPD experiments were conducted in a separate UHV setup consisting one chamber for both preparation and analysis[59, 60]; a picture is shown in Fig. 3.3. Briefly, the chamber houses LEED optics, a simple laboratory XPS setup that includes an electron analyzer and an X-ray source (Al Kα), a sputter gun and a quadrupole mass spectrometer (QMS) in a “Feulner-cup”[61] arrangement. Temperatures of 90 K may be reached using liquid nitrogen cooling from a reservoir on top. Resistive heating allows for temperature ramping.

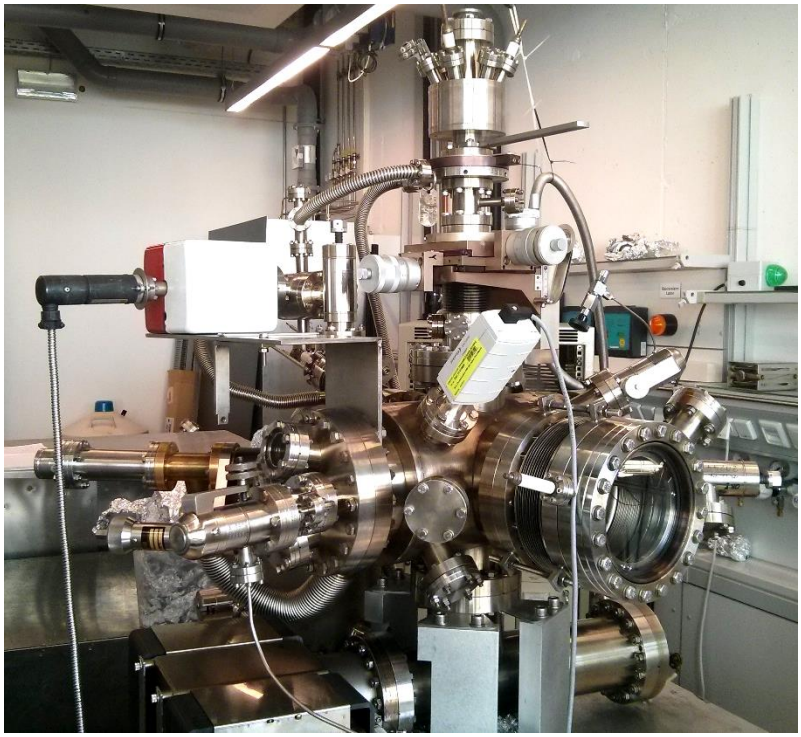

Fig. 3.3:*.Picture of the TPD machine.*

4 Surface reactions of Liquid Organic Hydrogen Carriers on Pt(111)

A number of compounds have been studied as a potential carrier molecule in the past.[62-65] This chapter focusses on the catalytic dehydrogenation (unloading) process of two material classes that are both promising candidates for hydrogen storage; see Fig. 4.1 for schematic drawings.

The first types are heterocyclic compounds, in particular the carbazole derivates N-ethylcarbazole (NEC), N-propylcarbazole (NPC) and N-butylcarbazole (NBC), hereinafter named N-alkylcarbazoles (NXC) when addressing all three carriers. These molecules can store additional 12 hydrogen atoms when hydrogenated to dodecahydro-N-alkylcarbazole (H_{12}-NXC), resulting in a hydrogen storage capacity of 5.8 wt% of the LOHC system in the case of NEC.[66] Hydrogenation is typically performed over supported Ru catalysts, while for dehydrogenation reaction mainly supported Pt or Pd catalysts are used.[67, 68] Major research activities have been focused on the LOHC system H_{12}-NEC/NEC, showing its applicability and thermal stability.[64, 69, 70] However, some features of this system complicate rapid implementation, including the limited technical availability and the relatively high melting point (68°C) of NEC.[15]

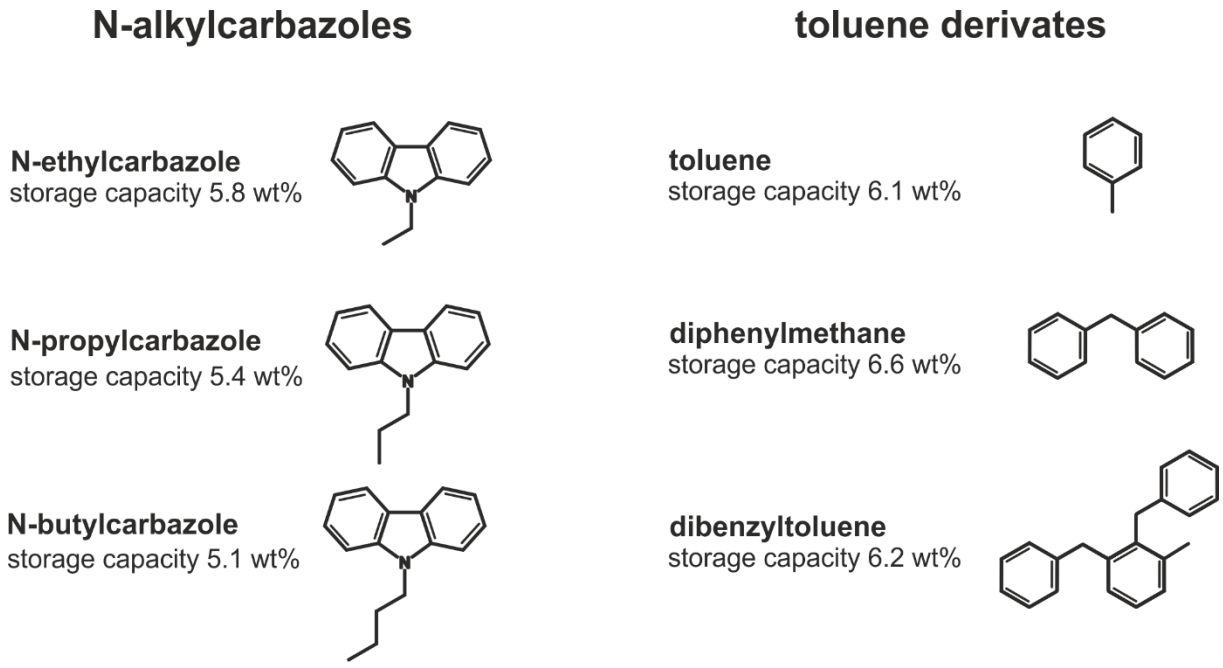

Fig. 4.1: *Schematic drawings of the investigated molecules. Carbazole derivates are depicted on the left hand side, toluene derivates are shown on the right hand side.*

The second types are benzene derivates, which contain only carbon and hydrogen atoms. It has been recently shown that mixtures of isomeric benzyltoluenes (e.g., Marlotherm LH; MLH) and dibenzyltoluenes (e.g., Marlotherm SH; MSH) can be used as LOHC system.[15] They offer some advantages compared to the heterocyclic carbazole derivates, such as their excellent technical

availability and full toxicological and ecotoxicological characterization, due to their application as industrial heat transfer oils. However, the heat of dehydrogenation of the system H_{12}-MLH/MHL and H_{12}-MSH/MSL is higher (71 $kJmol_{H2}^{-1}$) compared to the H_{12}-NEC/NEC system (55 $kJmol_{H2}^{-1}$), indicating that dehydrogenation is less favorable thermodynamically. This leads to higher temperatures needed for the reaction. In this thesis, the smaller molecules toluene and diphenylmethane serve as model systems for the chemical more complex systems based on MLH and MSH.

4.1 Surface reaction of Dodecahydro-N-ethylcarbazole on Pt(111)[P1]

One challenge in model approaches in surface science is the large size and low symmetry of molecules such as the NXCs.[41] Regardless of this fact, in this work it is shown that obtaining a molecular understanding of the fundamental surface processes during reaction is possible.[19, 71, 72] However, to succeed in such a demanding analysis, a combination of different experimental methods, and input from theory is needed. Here, only the HR-XPS results are discussed in detail.

To begin with, the dehydrogenation reaction and the side reactions of H_{12}-NEC on the Pt(111) surface are addressed. The starting point of our discussion is the adsorption of the molecule on the clean surface at 140 K. The surface is exposed to ~$4 \cdot 10^{-9}$ mbar of H_{12}-NEC and by continuously measuring both the C 1s and N 1s core levels this process is followed in detail; see Fig. 4.2e and f for selected spectra of this experiment and color-coded density plots of the full data sets in Fig. 4.2a and b. The growing peaks at a binding energy of 284.5 eV in the C 1s region and at 401.3 eV in the N 1s region are attributed to the molecular adsorption of H_{12}-NEC. At higher exposures, we find a second signal at 399.5 eV in the N 1s region, while in the C 1s region a broadening and a shift to higher binding energies is observed. This is due to the physisorbed multilayer of H_{12}-NEC on top of the chemisorbed monolayer. The quantitative analysis of the experiment in the N 1s region is presented in Fig. 4.3a. At its maximum, the monolayer corresponds to ~1.0 C monolayers (ML) per Pt atom on the surface. At exposures above 3 L, a decrease of the monolayer intensity is observed. This is due to damping of the monolayer signal by the multilayer on top of it.

Next, the heating experiment (TPXPS) is discussed. It was conducted subsequently to the adsorption experiments by applying a constant heating rate of 0.5 K/s while continuously measuring XP spectra. Selected spectra are shown in Fig. 4.2c (C 1s) and Fig. 4.2d (N 1s). The quantitative analysis is found in Fig. 4.3b. Note that the difference at the beginning of the heating experiment and the end of the adsorption experiment is due to postadsorption after closing the

valve. Above 240 K, a pronounced decrease of the peak at 399.5 eV in the N 1s region is observed. This indicates desorption of the multilayer, and is accompanied by the disappearance of the damping, i.e., by an increase of the monolayer signal at 401.6 eV. In the C 1s region, the broadening discussed above is reversed and the peak position is again found at 285.2 eV, which is due to a (closed) single layer of H_{12}-NEC.

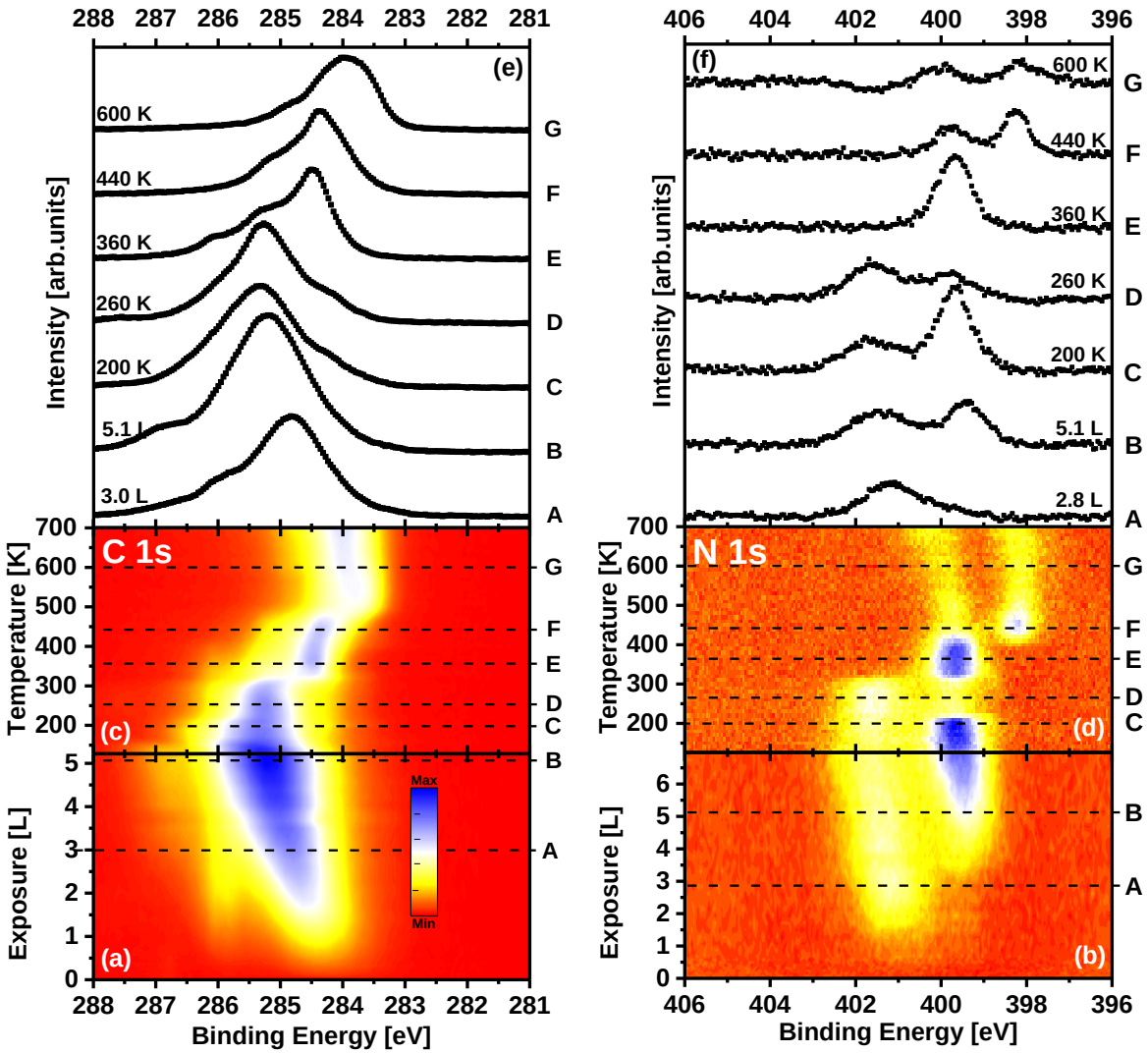

Fig. 4.2: *XP spectra recorded for adsorption and reaction of H_{12}-NEC on Pt(111). In (a) and (c) the C 1s spectra of adsorption and heating experiment (TPXPS), and in (b) and (d) the respective N 1s spectra are shown in a color-coded density plot. A-G indicate the selected spectra shown in the upper panels (e) and (f).*

Starting at 200 K, new signals develop in both core levels, indicating the first dehydrogenation step of the molecule. In the N 1s region, a peak appears at 399.5 eV, while in the C 1s region a lower binding energy shoulder is found at 284.5 eV. At 300 K these peaks strongly increase. The

strong change in the binding energy in the N 1s region (by 2.1 eV) indicates a major change in the bonding situation of the nitrogen atom. As discussed already for the reaction on Pd[68, 73], it is suggested that the first reaction occurs at the carbon atoms surrounding the nitrogen atom, that is at the α-carbon atoms of the pyrrole ring. In the N 1s region, the intensity remains unchanged between 330 and 390 K (see also Fig. 4.3b). Obviously, no further changes at the pyrrole ring are found in this temperature range. If also the β-carbon atoms are abstracted already at 330 K, H_8-NEC is the first intermediate of the reaction, as already suggested in previous studies.[73, 74] In the C 1s spectra in Fig. 4.2c one finds a further increase of the peak at 284.5 eV at cost of the higher binding energy peak at 285.2 eV between 330 and 390 K. This behavior is assigned to stepwise dehydrogenation of H_8-NEC to NEC at the outer benzene entities.

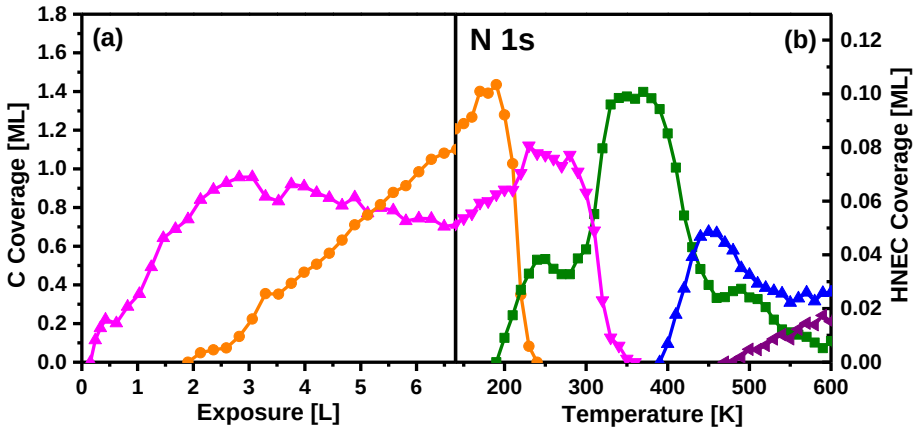

Fig. 4.3: *Quantitative analysis of the HR-XPS experiments with H_{12}-NEC in the N 1s core level shown in Fig. 4.2b; (a) shows the adsorption experiment and (b) shows the heating experiment (TPXPS)*

Above 390 K, a new peak at 398.1 eV appears in the N 1s region. This indicates the dealkylation reaction of NEC to carbazole. Though carbazole can be reversibly hydrogenated under similar conditions as NEC[15], it exhibits a considerably higher melting point. Therefore, this is an unwanted reaction, since in a technical process the melting point of the LOHC mixture increases as well.[15, 73] The carbazole signal reaches its maximum at 450 K, after which it drops and other species appear that are assigned to further (unidentified) decomposition products. Heating to even higher temperatures (up to 1000 K) leads to formation of carbon (and nitrogen) fragments on the surface (data not shown). In Fig. 4.4 a scheme of the proposed surface reaction is depicted.

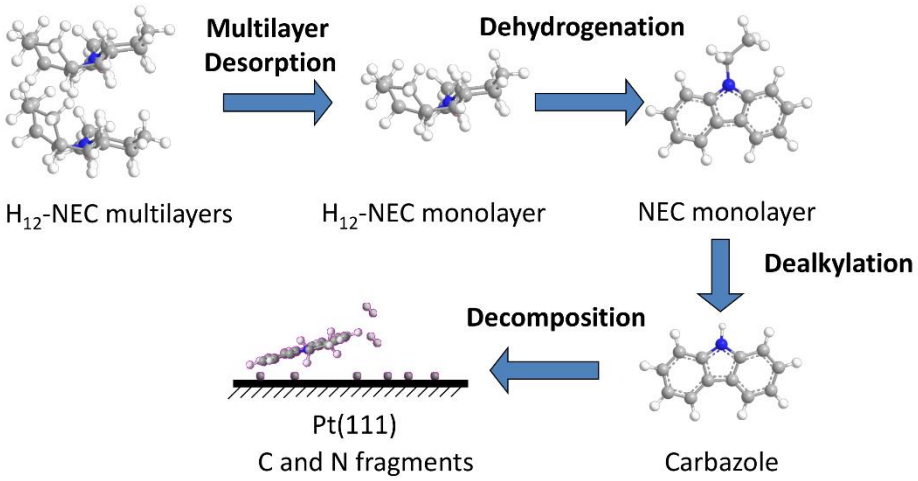

Fig. 4.4: *Surface Reaction Scheme of H_{12}-NEC on Pt(111)*

4.2 Temperature-Programmed Reaction study of Dodecahydro-N-ethylcarbazole on Pt(111)[P2]

The results in the last chapter provide a detailed understanding of the reaction on the Pt(111) surface under UHV conditions. Under reaction conditions, however, the mechanism and kinetics may differ from the one obtained in UHV. Therefore it is essential to probe the surface reactivity during exposure to the molecule, while heating the surface. Temperature-programmed reaction (TPR) studies are used to obtain such information.[71, 75] XPS is used to monitor the surface species during the heating ramp.

In contrast to the last chapter, adsorption of H_{12}-NEC (~$8 \cdot 10^{-9}$ mbar) is performed at a higher temperature (250 K) (to prevent multilayer adsorption) until saturation is reached, and subsequently the sample is heated during continuous supply of the reactant. Again, during the experiment XP spectra were recorded continuously both in the C 1s and N 1s regions.

To begin with, during adsorption at 250 K the N 1s spectra (data not shown) show a peak at 401.6 eV that is due to H_{12}-NEC and one at 399.8 eV that is attributed to the partially hydrogenated product H_8-NEC, similar to our findings in the previous chapter. A quantification of both species shows a ratio of about (H_8-NEC) 4:6 (H_{12}-NEC). Most probably dehydrogenation of all species to H_8-NEC is suppressed at saturation due to space limitations on the surface. The C 1s spectra (data not shown) exhibit a peak at 285.2 eV that is due to contributions from the CH_2 subunits, and a smaller shoulder at 284.1 eV attributed to the CH subunits of the partially

dehydrogenated molecules. Fig. 4.5 shows the quantitative analysis of the experiment in the C 1s region.

Next, the thermal evolution of the surface species is discussed. In fact, the surface chemistry is similar to the observations found in Chapter 4.1, aside from difference in the total coverage. The analysis of the N 1s region shows that H_{12}-NEC vanishes completely at 340 K, indicating complete dehydrogenation of the pyrrole ring. No further changes are observed up to 390 K. However, from the C 1s data in Fig. 4.3 it is obvious that it takes up to 380 K for the reaction to complete. The dehydrogenation process from H_8-NEC to NEC is only visible in the C 1s core level, because it affects the carbon atoms other than the ones of the pyrrole ring.

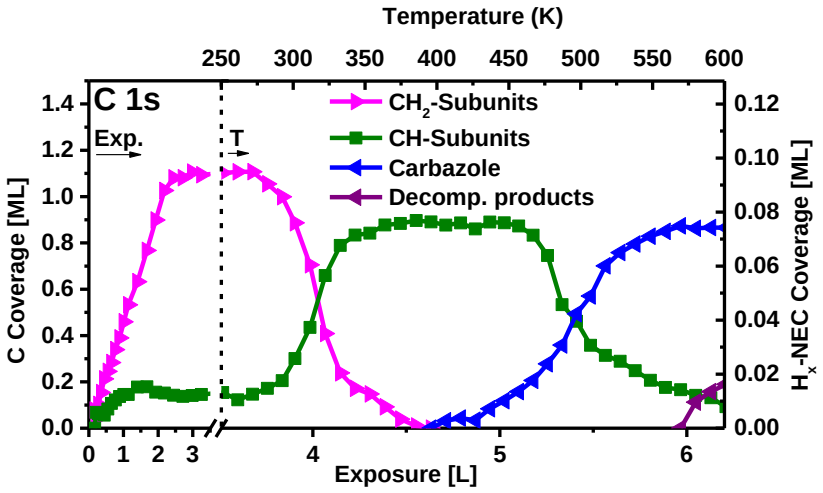

Fig. 4.5: *Quantitative analysis of the TPR experiment as monitored by XPS in the C 1s core level. The dashed line marks the start of the heating ramp.*

At 380 K, the reaction is completed, and only NEC is found on the surface. Above 390 K, the dealkylation reaction starts. This strongly affects the nitrogen atom, but in the C 1s region only a minor peak shift and a broadening of the signal is observed. Probably a large number of different surface species, such as the alkyl chain and carbazole, leads to the broadening. Further dehydrogenation and other decomposition is observed at even higher temperatures and the total intensity rises. This is probably due to an increasing packing density of the decomposition products on the surface by continuous dosing.

Additional information on the adsorption and desorption behavior was acquired using temperature-programmed molecular beam (TPMB) experiments. With this method it is possible to explore the reactivity at different temperatures during continuous supply of the reactants by tracing the dehydrogenation and decomposition products in the gas phase. The results from these studies show that the product distribution in the gas phase differs strongly from the surface

products found using XPS. Interestingly, up to 400 K the dehydrogenation and decomposition products H_8-NEC and H_8-carbazole (an unwanted, dealkylated molecule) are the dominant molecules found in the gas phase. The fact that desorption of the more strongly dehydrogenated products such as NEC is suppressed is attributed to their stronger interaction with the surface, most probably caused by the flat shape of the molecule, and strong π-bonding.[68, 76]

4.3 Alkyl chain-length dependent surface reaction of dodecahydro-N-alkylcarbazoles on Pt(111)[P3]

In order to find an optimum LOHC system, a balance between storage capacity, stability and physicochemical properties of the molecule has to be found. NEC is able to store 5.8 wt.% of hydrogen when fully hydrogenated to H_{12}-NEC[77, 78], but exhibits a relative high melting point of 68°C. Lowering the melting point is possible by elongating the alkyl chain. Due to entropic reasons, replacing the ethyl group by an N-propyl group, and therefore using N-propylcarbazole (NPC) instead of NEC, leads to a lowering of the melting point to 48°C. Moreover, eutectic

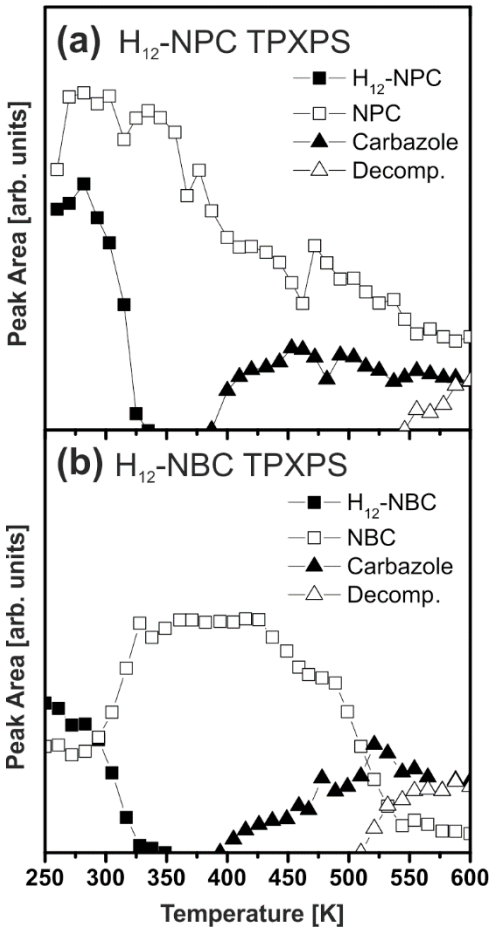

Fig. 4.6: *Quantitative analysis of the heating experiments (a) H_{12}-NPC and (b) H_{12}-NBC on Pt(111) in the N 1s core level.*

mixtures of NEC and NPC show even lower melting points.[79] The drawback of using NPC as LOHC is that the storage is reduced by 0.4 % due to the longer alkyl chain, which does not participate in the hydrogenation/dehydrogenation cycles.

Here, the effects of the alkyl chain length on dehydrogenation behavior and the unwanted dealkylation reaction are discussed. The heating experiments give information about whether the surface reactivity is different for the three carriers. For the heating ramps, the molecules NEC and NBC were adsorbed at 250 K to prevent multilayer adsorption. In the case of NPC, the sample was heated to 250 K after adsorption at 140 K to desorb the multilayer prior to the heating ramp. The quantitative analysis of the experiments of NPC and NBC is shown in Fig. 4.6. The reaction of NEC was already discussed in great detail in Chapter 4.1. Aside from minor differences, the results for H_{12}-NPC and H_{12}-NBC show a similar picture. As evident from a comparison of Fig. 4.6 and Fig. 4.3b, at 250 K dehydrogenation has proceeded to about the same extent. Upon heating, the signals of the dehydrogenated species increase at the cost of the H_{12}-NXC signals. At 330 K, there is only one peak found in the N 1s region for NXC. Up to ~375 K, stepwise dehydrogenation finished and only the dehydrogenated carriers are left (deduced from the C 1s region).

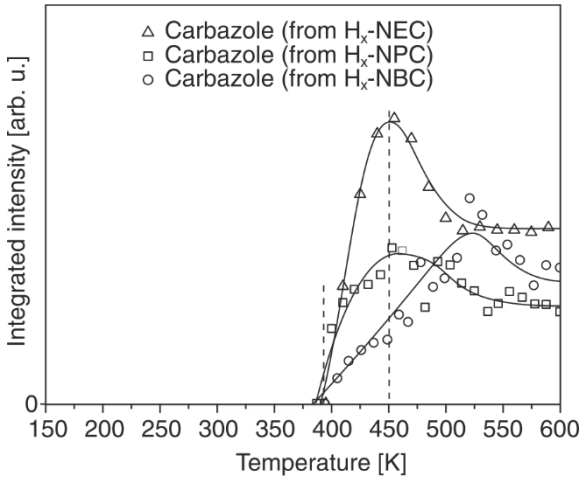

Fig. 4.7: *Integrated intensities of the N 1s peak assigned to carbazole in the reaction of H_x-NXC on the Pt(111) single crystal*

Starting at 380-390 K, the unwanted dealkylation reaction is observed in all three cases by the appearance of the N 1s peak at 398.1 eV at cost of the peak at 399.5 eV. A comparison of the decrease in the quantitative analysis in Fig. 4.7 reveals a clear trend to lower reactivity with increasing alkyl chain length. At 450 K, ~70% of NEC is converted to carbazole, while NPC yields ~40%, and NBC reacts to an even lower extent, yielding 20%. Interestingly, the amounts

found above 500 K do not reveal any clear trend. At even higher temperatures, further decomposition is observed for NPC and NBC, in line with the findings for NEC.

In conclusion, all carbazole derivates H_{12}-NXC show similar reactivity towards dehydrogenation and also similar stability towards dealkylation, rendering them all suitable for practical use as LOHC in a system for renewable energy storage.

4.4 Thermal stability of Dodecahydro-N-ethylcarbazole on Pd(111)[P4]

The studies of H_{12}-NEC on Pt(111) led to a profound understanding of the surface reaction. Since Pd is also a catalyst applied in dehydrogenation reactions[80], investigations of the dehydrogenation mechanism were performed also on the Pd(111) surface. The reaction mechanism was elucidated using IRAS and HR-XPS experiments under surface science conditions and by density functional theory (DFT) calculations.[81] Here only the HR-XPS experiments are discussed.

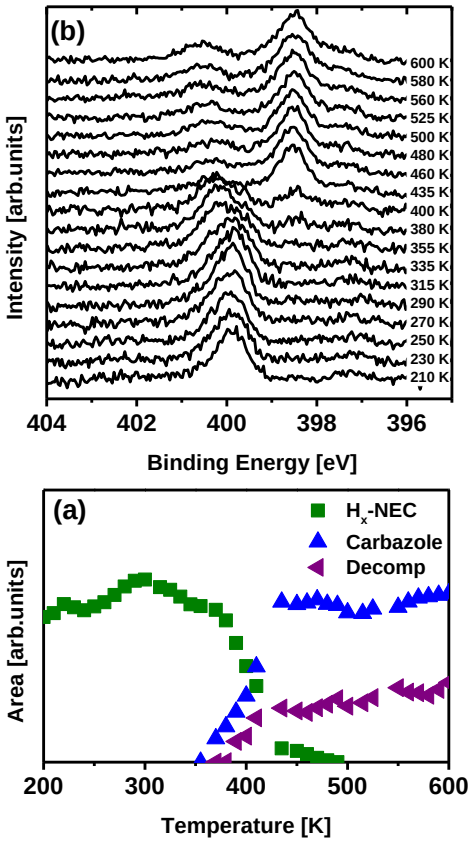

Fig. 4.8: *(a) Selected N 1s spectra of the TPXPS experiment of H_{12}-NEC on Pd(111). (b) Quantitative analysis of the experiment shown in (a).*

Separate adsorption and heating experiments have been performed for the C 1s and N 1s core levels. In the adsorption experiment conducted for the N 1s (C 1s) region, 1 L (1.4 L) of H_{12}-NEC

was adsorbed on the Pd(111) surface at 200 K. Molecular adsorption, as verified by IRAS[81], is observed by a peak at 399.9 eV in the N 1s region and a broad peak at 286.0 eV in the C 1s region.

Subsequent to the adsorption, heating experiments at a rate of 0.5 K/s were conducted. In Fig. 4.8b, selected N 1s spectra are shown. Up to 350 K, no pronounced changes are observed. Interestingly, from the IRAS analysis (see [P4]), it is known that above 223 K dehydrogenation to H_8-NEC occurs. In the N 1s region, no changes are observed during dehydrogenation to H_8-NEC. Consequently, in the quantitative analysis (Fig. 4.8a) the signal at 399.9 eV is named "H_x-NEC" (where *x=0-12*). However, in the C 1s region (data not shown) minor peak shifts and changes of the spectra are observed during dehydrogenation, but no unambiguous assignment to one of the dehydrogenation products is possible.

Starting at 350 K, changes in the N 1s spectra are observed: a peak appears at 398.5 eV and an additional small peak at 400.5 eV is found. A comparison to the findings on Pt(111) (see Chapters 4.1 - 4.3) shows that the peak at 398.5 eV is due to dealkylation, leading to carbazole. Moreover, the peak at 400.5 eV is due to a second decomposition reaction near to the nitrogen atom of the pyrrole ring. Up to 600 K, these two species are stable, which is also confirmed by data in the C 1s core level. Above 600 K (data not shown), a further increase of the peak at 400.5 eV is observed, which hints at further decomposition.

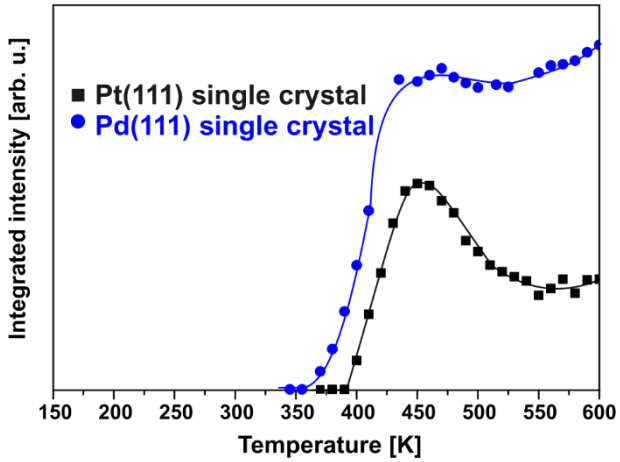

Fig. 4.9: *Comparison between the integrated intensity of the dealkylation product on the Pt(111) and Pd(111) surfaces that is generated during heating of H_{12}-NEC.*

In conclusion, the study on Pd(111) in UHV showed that the thermal stability of NEC is lower by ~30 K on Pd(111) than on Pt(111); in Fig. 4.9 the evolution of the decomposition products is compared. The lower dealkylation temperature is a drawback of the dehydrogenation reaction with Pd compared to Pt as catalyst, since dealkylation needs to be avoided in the hydrogen storage cylces of H_{12}-NEC/NEC under industrial condition.

4.5 Dicyclohexylmethane(DCHM)/Diphenylmethane(DPM) on Pt(111)[P5]

In the analysis of the carbazole derivates, the information of the single nitrogen atom in the pyrrole ring was the key to understand the changes in the C 1s spectra, and thus to clarify the reaction mechanism. For the case of hydrocarbons, however, the analysis becomes more challenging, as these molecules only contain carbon and hydrogen atoms. In order to overcome this challenge, the combination of a variety of experimental surface science methods is used. In total, four experimental techniques were applied: TPD, HR-XPS, IRAS and NEXAFS.

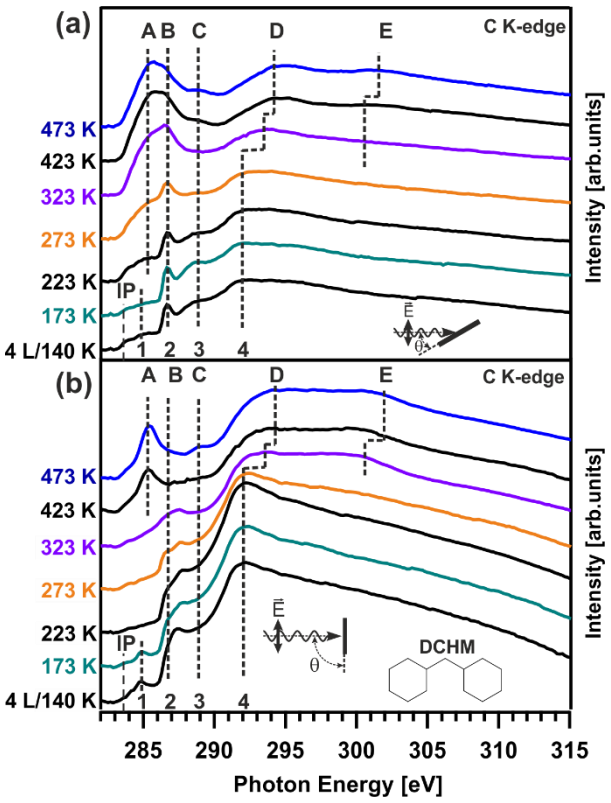

Fig. 4.10: *The carbon K-shell NEXAFS spectrum of DCHM on Pt(111) for various temperatures. In (a) the grazing incidence specta (20°), and in (b) the normal incidence (90°) spectra are shown.*

Here, the surface reactions of DCHM are discussed in brief using the NEXAFS results. In Fig. 4.10, spectra both in gracing incidence (GI, 20°) and normal incidence (NI, 90°) are shown. The molecule was adsorbed at 140 K; spectra were taken at an exposure of 4 L (black curves labelled "4 L/140 K" in Fig. 4.10). A small feature ("1" in Fig. 4.10) is due to an effect[82] of the interaction between the molecule and the substrate. The resonances (2) found at 287 eV in NI and 286.6 eV in GI are attributed to mixed Rydberg/valence[82] π* states of the CH_2 groups. We are unable to assign the resonance found at 288.9 eV (3, more pronounced in GI). The main feature

(4), found at 285 eV both in GI and NI, is attributed to the σ* orbitals characteristic for saturated hydrocarbons such as (cyclo)alkanes, and also DCHM. In Fig. 4.11 (step "1") a schematic drawing of the adsorption situation of DCHM is shown.

Next, the sample was heated to selected temperatures for 1 min and subsequently NEXAFS measurements were conducted. In the spectrum at 223 K, the small peak at 285.0 eV in NI disappears, while in GI we find an increasing contribution at this energy, indicating a π* resonance that is due to the formation C=C double bonds.[49] This contribution increases further at 273 K, while in NI there is no resonance at this position, which indicates the formation of a C=C double bond that is planar to the surface. Together with the other techniques, it is possible to assign this reaction to the partial dehydrogenation of cyclohexyl rings to form a double π-allylic surface intermediate (see step "2" in Fig. 4.11). Note that exact position of the C=C double bonds in the two π-allyls cannot be deduced from the data; the schematics in Fig. 4.11 are proposed intermediates.

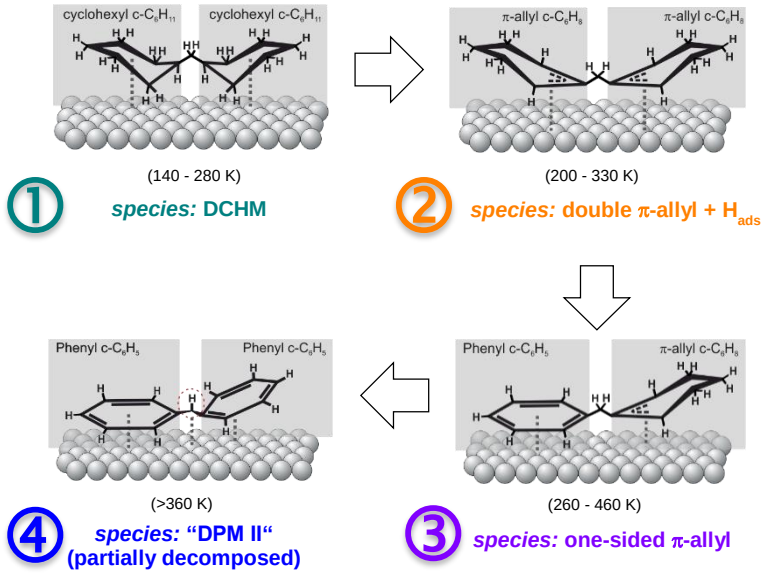

Fig. 4.11: *Schematic drawing of the proposed reaction steps of DCHM on Pt(111).*

In the spectrum at 323 K, a further increase of the π*-state is found at 285.0 eV in GI, while in NI still no increase occurs at this photon energy. Moreover, in NI we find the appearance of a resonance at 300.5 eV, indicating the formation of a phenyl ring[49]. We identify a one-sided π-allylic species (see step "3" in Fig. 4.11): one of the two remaining π-allylic C_6H_8 groups dehydrogenates to form a phenyl ring, while to other stays intact. All C=C double bonds are still in-plane with the surface, as deduced from IRAS.

Above 423 K, a π* state appears also in NI and a change in the relative intensities of π* and σ* occurs, indicating a change in adsorption geometry while further dehydrogenation occurs. The spectra look very similar to benzene[50, 83], but relative intensities of the π* resonances in GI and NI show that at least one phenyl ring must be bent away from the surface (see step "4" in Fig. 4.11). The resulting species is close to diphenylmethane (DPM), the hydrogen-lean molecule in the LOHC system DCHM/DPM, therefore it is denoted “DPM II”. However, during this reaction step, C-H bond scission at the methylene group probably occurs, as suggested from the XPS and TPD results.

To summarize this chapter, we studied the adsorption behavior and clarified the reaction steps of the LOHC system DCHM/DPM on the Pt(111) single crystal. The results show that dehydrogenation of cyclohexyl groups proceeds in steps by forming π-allylic intermediates, and that decomposition at high temperatures most likely happens by hydrogen abstraction at the methylene group.

5 Carbide-modified molybdenum model catalysts

To replace expensive platinum catalysts by cheaper materials, competitive alternatives need to be found.[33] Transition metal carbides (TMCs) show similarities in the catalytic behavior to those of Pt-group metals.[34] The formation of TMCs is induced by dissolution of carbon in the parent transition metal. In this process, carbon is incorporated into the interstitial sites of the crystal lattice,[84] leading to changes in the chemical and physical properties compared to the pure transition metal catalyst.[35, 85, 86] Investigations have shown that hydrogenation and dehydrogenation, as well as hydrogenolysis reactions of hydrocarbons on TMCs indeed show similarities to the Pt group metals (Ru, Rh, Pd, Pt, Ir)[35, 87], while very different reactions have been reported for oxygen-containing molecules.[88]

There are two ways of obtaining highly defined transition metal carbide surfaces under surface science conditions. One way is to use bulk carbide single crystals, another is to produce carbide-modified single crystals of transition metals. Surfaces formed in the latter process involve uncertainties concerning the exact surface structure of the carbide layers and often display defects[35], imperfect terminations, and some of them show surface reconstruction.[89, 90] However, the advantage of using the carbide-modified surfaces lies in the possibility to tune the carbon content from zero up to the stoichiometric amount of the bulk carbide.

Extensive studies have been conducted for the carbide overlayers of the group VI metals molybdenum and tungsten.[35, 86] Their preparation involves exposure to unsaturated hydrocarbon gases at elevated temperatures (typically ethylene at ~900 K), which induces cracking of the molecules, resulting in carbon layers on the surface.[90, 91] Subsequent annealing to temperatures above 1100 K leads to diffusion of the carbon into the bulk and to formation of the preferred stoichiometry of the produced phase (W_2C, Mo_2C, WC,…).[86, 92-94] Moreover, preparation can also be performed by simply heating a carbon-containing crystal[95], or by directly exposing a clean crystal to carbon above 1100 K.[90]

In this work, fundamental studies on the preparation and comparison of the carbide-modified Mo(100) and Mo(110) single crystal surfaces, and a study on the adsorption and reaction of CO on C/Mo(110) have been performed. These investigations aim at providing a basis for future investigations of dehydrogenation reactions of LOHCs on such catalysts.

5.1 Comparison of the carbide-modified surfaces C/Mo(110) and C/Mo(100)[P6]

This chapter is concerned with the a comparison of the carbide-modified surfaces of the Mo(100) and Mo(110) single crystals. In the in situ experiments, carburization was performed by exposure to ethylene, and subsequently the carbides were removed by exposure to oxygen. These results are compared to first principle calculations using DFT.

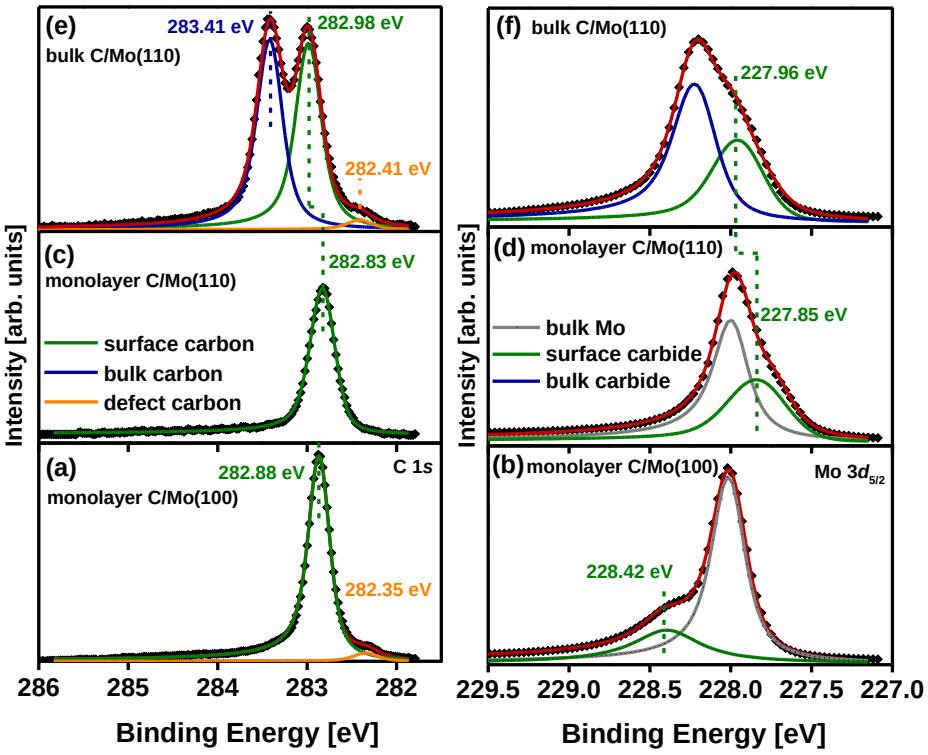

Fig. 5.1: *Comparison between different carbide overlayers. In (a) the C 1s and (b) the Mo $3d_{5/2}$ core level spectrum of the monolayer carbide prepared on Mo(100) is shown. In (b) and (c) the respective spectra of the monolayer carbide on Mo(110) are shown. In (e) and (f), the spectra of the bulk carbide on Mo(110) are displayed.*

First the findings for the monolayer carbide on Mo(100) are discussed. This is a single carbide layer situated on the first layer of the single crystal substrate. At 1200 K, we monitored the transformation of a partly oxygen covered surface up to saturation (at ~1.5 L) of the monolayer carbide peaks by the exposure to ethylene at a pressure of $1.4 \cdot 10^{-8}$ mbar using HR-XPS in the C 1s and Mo $3d_{5/2}$ regions; for the complete data set see [P6]. In Fig. 5.1a and b, the spectra at 140 K after the preparation are shown. In the C 1*s* region, a sharp peak at 282.88 eV and a small one at 282.35 eV are observed. For the main peak, a coverage of 0.95 ± 0.10 ML carbon atoms per Mo surface atoms is found. In the Mo $3d_{5/2}$ region, a metallic bulk peak at 228.00 eV and a carbide peak at 228.42 eV are found. The layer showed a (1×1) LEED pattern at saturation of the

monolayer carbide, as also discussed in ref. [96]. In a similar system, the $Mo_{0.75}Re_{0.25}(100)$ alloy[97], carbon occupies all four-fold hollow sites of the (100) facet. Most probably, on the Mo(100) crystal the same adsorption sites are occupied (see Fig. 5.2). This suggestion has been made already in previous studies[98, 99] and is supported by our DFT calculations[P5]. Consequently, the main peak at 228.88 eV in the C 1s core level is assigned to carbon atoms in the four-fold hollow sites, and the peak at 228.42 eV in Mo $3d_{5/2}$ spectrum is due to the first layer molybdenum atoms. Furthermore, we assign the small C 1s peak at 282.41 eV to surface defects.

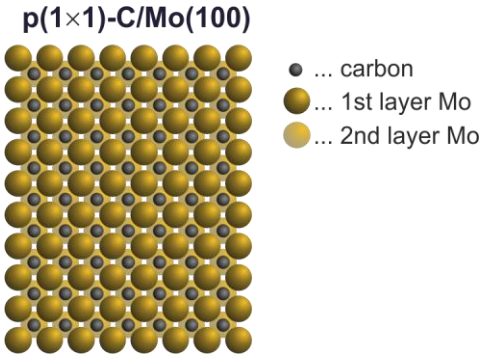

Fig. 5.2: *Surface structure of the monolayer carbide on Mo(100) (coverage 1.0 ML).*

The preparation of a bulk carbide on Mo(100) was first tried by simply raising the ethylene pressure during carburization to above $1.7 \cdot 10^{-6}$ mbar. Even for ethylene doses of larger than 2000 L only a very slow growth of a bulk carbide peak is observed (not shown). Therefore, a different route was followed: dosing ethylene at 900 K followed by flashes to 1300 K.[91, 92] However, this preparation method most probably leads to faceting of the surface on Mo(100), and is not further discussed here.

In comparison to Mo(100), differences for the monolayer carbide on Mo(110) are observed both in the C 1s and Mo $3d_{5/2}$ regions (see Fig. 5.1c and d), and a (4×4) structure is found in LEED. In the C 1s spectra, only one single peak is found, corresponding to a coverage of 0.43 ± 0.06 ML. In the Mo $3d_{5/2}$ region, besides the metallic peak at 228.00 eV, a broader peak is found at 227.85 eV that is assigned to the monolayer carbide. Above 3.5 L, saturation of these peaks is observed. DFT calculations show that carbon most probably forms dimers in two neighboring three-fold hollow sites. A possible structure that exhibits a (4×4) structure and a carbon coverage close to findings in XPS (3/8 ML) is depicted in Fig. 5.3. In this structure, Mo atoms with two, one and no neighboring carbon atom(s) are found. The peak at 227.85 eV therefore is attributed to contributions from these molybdenum surface species.

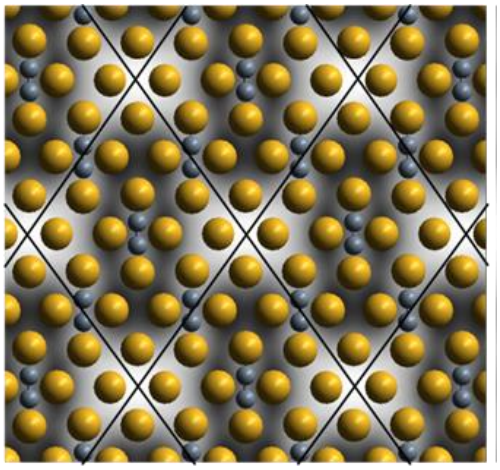

Fig. 5.3: *Suggested (4×4) surface structure of the monolayer carbide on Mo(110) for a coverage of 3/8 ML (topmost layer, Mo atoms are depicted in gold, carbon atoms in grey). In the background, a calculated constant current STM image is shown.*

Interestingly, the bulk carbide could be prepared on Mo(110) at 1200 K by simply increasing the exposure of ethylene by orders of magnitude. After dosing ~13000 L ethylene and cooling down to 140 K, the spectra in Fig. 5.1e and f are observed. In the C 1s region, the surface peak shifts to 282.98 eV. We find a coverage of 0.55 ± 0.05 ML carbon atoms per Mo surface atom. An additional bulk Mo_2C peak appears at 283.41 eV and a small defect peak is found at 282.41 eV. In the Mo $3d_{5/2}$ region, the surface contribution shifts to 227.96 eV, while the metallic contribution vanishes and a bulk Mo_2C appears at 228.23 eV.

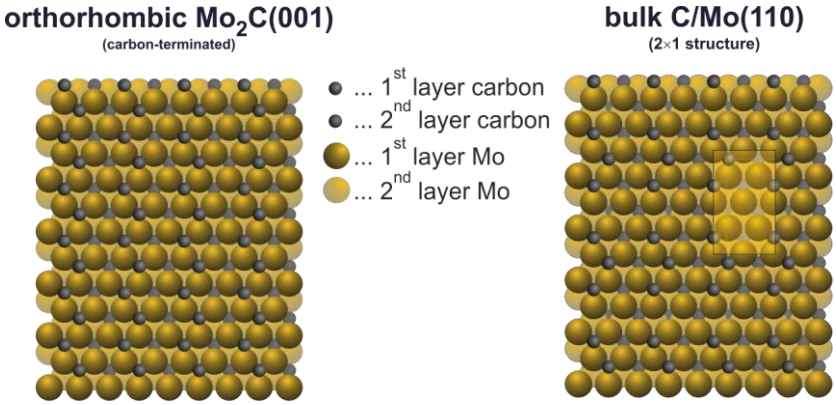

Fig. 5.4: *(a) Carbon-terminated bulk orthorhombic $Mo_2C(001)$ structure; (b) Suggested 2×1 surface structure for the bulk carbide on Mo(110). See the text for details.*

The results from DFT calculations show that for the bulk carbide no dimers form on the surface. The structure is most probably very close to what is found for the carbon-terminated (001) surface of orthorhombic Mo_2C[35, 100-102], where single carbon atoms occupy the three-fold hollow site of the quasi-hexagonal Mo lattice (see Fig. 5.4a). Interestingly, similar to the monolayer carbide, the

bulk carbide shows a (4×4) structure in LEED, though with an increased background intensity. A (4×4) structure was also found by Clair et al.[103] for the C-terminated orthorhombic $Mo_2C(001)$ surface. They suggested that three (2×1) orthorhombic domains (see Fig. 5.4b) rotated by 120° lead to the observation in LEED.

To conclude, the combined DFT and *in situ* XPS study provides insight in the surface structure of the carbide-modified C/Mo(100) and C/Mo(110) surfaces, and thus constitutes an important basis for the study of chemical reactions on these substrates.

5.2 Surface reactivity of C/Mo(110) towards CO[P7]

The reactivity of oxygen-containing molecules on TMCs is known to be different compared to the Pt-group metals.[88] Of particular interest is the reactivity towards CO, as poisoning effects play a critical role in catalysis. In general, the molecular desorption temperature of CO is lower on TMCs than on Pt-group metals, which hints at a higher resistance towards CO poisoning.[35, 88] In this study, the influence of the carbide content, i.e. the carbide thickness, on the surface reaction of CO is investigated. On the monolayer carbide and bulk carbide on Mo(110), as prepared by the methods described in Chapter 5.1, adsorption experiments were performed at 140 K, followed by HR-XPS. Subsequently, heating experiments were conducted to study the surface reactions, and in addition TPD experiments were carried out to monitor the desorbing gases during reaction. However, only the XPS data is discussed here; for the TPD data see [P7].

First, the adsorption and reaction of CO on the monolayer carbide is discussed. The surface was monitored using XPS in the C 1s, O 1s and Mo 3d core levels (in separate experiments) while it was exposed to CO at a pressure of $5 \cdot 10^{-9}$ mbar at 140 K. Fig. 5.5a shows the quantitative analysis of the experiment in the O 1s core level. Before adsorption (at 0 L), no oxygen is found on the surface, and the carbide shows the spectra as depicted in Fig. 5.1c and d. During exposure, CO species are found at 531.5 eV (CO_{M2}) and 532.5 eV (CO_{M3}). Note that a third species (CO_{M1}) is resolved in the C 1s region only; this species is not discussed here, since it is observed only at low exposures (see [P7]). In the spectra at 140 K, adsorbed oxygen is found with a peak at 530.3 eV, which is due to dissociation of CO. Note that a similar behavior is also found on pristine Mo(110).[104] At saturation, CO_{M2} and CO_{M3} show coverages of ~0.4 ML and ~0.25 ML, respectively. Moreover, ~7% (0.05 ML) dissociate during adsorption. In the C 1s core level (data not shown), the peaks of the CO_{M2} and CO_{M3} species are found at binding energies of 285.5 and 286.0 eV, respectively.

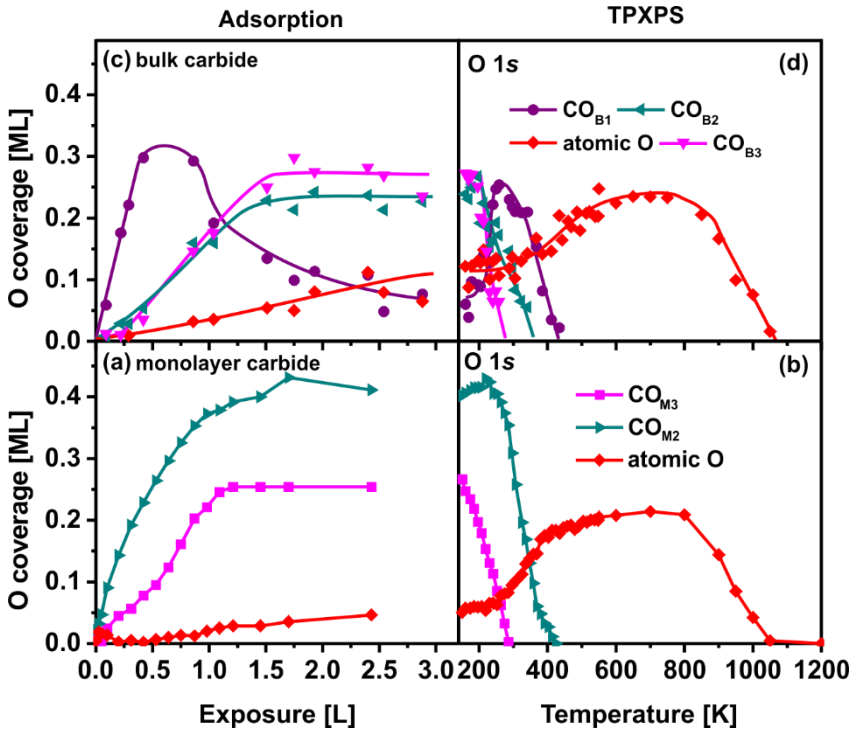

Fig. 5.5: *Quantitative analysis (O 1s core level) of the experiments with CO on the monolayer carbide (bottom) and bulk carbide (top) on Mo(110). In (a) and (c) the results of the adsorption experiments, and in (b) and (d) the results of the TPXPS are shown.*

Upon heating, CO_{M3} immediately starts to decrease and vanishes at 300 K. Starting at 260 K, the species CO_{M2} also decreases, while the amount of atomic oxygen increases, which is due to thermally activated dissociation of CO. This process finishes at ~400 K; at the same temperatures as CO_{M2} has disappeared; a comparison of the total amounts before and after desorption show that approx. 0.15 ML of CO_{M2} dissociate in this step. In the range of 800 - 1150 K, the atomic oxygen signal decreases due to associative desorption of CO (see the TPD discussion in [P7]). By heating above 1150 K, the state of the carbide overlayer before the adsorption experiment is restored.

Next, the adsorption experiment at 140 K on the bulk C/Mo(110) surface is discussed. Fig. 5.5c shows the quantitative analysis in the O 1s core level. Three molecular species $CO_{B1\text{-}B3}$ are found. Up to 0.5 L, the species CO_{B1} dominates, and reaches a maximum at a coverage of ~0.3 ML. Interestingly, above 0.5 L this species is increasingly suppressed due to lateral interactions to a coverage of ~0.07 ML at saturation, while CO_{B2} and CO_{B3} increase to values of ~0.2 and ~0.25 ML, respectively. The total coverage of molecular CO at saturation is ~0.6 ML, while ~0.1 ML of CO adsorb dissociatively.

During heating, the CO_{B2} and CO_{B3} species desorb up to 380 K. Interestingly, CO_{B1} increases to ~0.25 ML up to 260 K, indicating that the lateral interactions are reduced, leading to the increase of the peak. This is the reverse process to what was found during adsorption. Between 300 and 460 K, ~60-70% of CO_{B1} dissociate and ~30-40% desorb. Above 460 K, only atomic oxygen and carbon (each ~0.25 ML) are adsorbed. Starting at 800 K, we find a decrease of the overall surface coverage, which is due to the associative desorption of carbon and oxygen as CO. This leads to a "clean" carbide surface as prepared before the adsorption experiments.

In conclusion, the reactivity of monolayer and bulk carbide are quite similar, but show some distinct differences concerning the adsorbed species and the reactivity towards dissociation. These studies provide for the basic knowledge needed for future experiments with LOHCs on molybdenum carbide.

6 Summary

Efficient energy storage systems have to be developed in order for renewable energy sources to replace today's predominantly used carbon-based fossil fuels. Among suitable compounds for energy storage, hydrogen exhibits the highest gravimetric storage density (33 kWh/kg), but present physical hydrogen storage methods include either high pressures or cryogenic temperatures. One alternative concept is to store hydrogen in organic molecules, so-called liquid organic hydrogen carriers (LOHCs).

Surface science studies give fundamental insight in the nature of heterogeneous catalysis on surfaces. In this work, a number of powerful experimental techniques (see Chapter 3) were used to study the dehydrogenation and decomposition LOHCs on the atomically well-defined Pt(111) and Pd(111) single crystals in ultra-high vacuum (UHV). It is demonstrated that synchrotron-based spectroscopic methods are excellent tools to study reactions even of large molecules such as LOHCs on surfaces. Third generation synchrotron sources, such as BESSY II at the Helmholtz-Zentrum Berlin (HZB), provide highly intense X-ray radiation at low spectral line width. This allows for fast high-resolution X-ray photoelectron spectroscopy (HR-XPS) experiments, and thus to follow chemical reactions which happen at a timescale of seconds. The mechanistic understanding of the LOHC model systems on a molecular level provides a basis to design catalysts and LOHCs on a knowledge-driven basis.

In this context, the surface reaction of the heteroatom-containing LOHC dodecahydro-N-ethylcarbazole (H_{12}-NEC) was studied on Pt(111) (see Chapter 4.1 and 4.2). The first reaction step involves desorption of the physisorbed multilayer up to 240 K, leaving the chemisorbed monolayer of H_{12}-NEC on the surface. Starting at 200 K, dehydrogenation is observed at the α- and β-carbon atoms in the pyrrole subunit; the resulting H_8-NEC is the first stable intermediate at ~330 K. In the next step, this species dehydrogenates stepwise at the outer benzene entities to NEC until 380 K. Above 390 K, C-N bond scission is observed, that is, the abstraction of the ethyl group from the molecule (dealkylation), leading to carbazole and other hydrocarbon fragments on the surface. This reaction leads to a deterioration of the LOHC system, and therefore it is detrimental. Carbazole is the dominant surface species at 450 K. At even higher temperatures, further dehydrogenation and the formation of carbon fragments occurs. This study illustrates that in a particular temperature range, H_{12}-NEC is a regenerable LOHC molecule, with 380 K being the ideal unloading temperature under surface science conditions.

In order to study the influence of the alkyl chain length on the surface reaction, in addition the NEC derivates dodecahydro-N-propylcarbazole (H_{12}-NPC) and dodecahydro-N-butylcarbazole (H_{12}-NBC) were studied on Pt(111) (see Chapter 4.3). The reaction follows the same steps as for NEC, and also the stability is the same, since for all three molecules dealkylation to carbazole starts at 380-390 K. Interestingly, a reactivity decrease towards dealkylation is observed for longer alkyl chains: at 450 K NEC shows a conversion to carbazole of roughly 70%, whereas NPC yields ~40%, and NBC only ~20%. However, the final amount of carbazole at ~500 K shows no clear trend. In conclusion, the overall dehydrogenation reaction and also the dealkylation are not affected by the different alkyl chain lengths.

To compare the results obtained on Pt(111) with other catalyst materials, the thermal stability of H_{12}-NEC on Pd(111) was investigated in Chapter 4.4. The HR-XPS results show that on Pd(111) the dealkylation reaction starts at 360 K, which is 30 K lower than on Pt(111). This hints to a lower activation energy of the reaction on Pd(111) compared to Pt(111), and might lead to a higher propensity for self-poisoning for Pd(111).

The tunable photon energy at synchrotron sources offers the possibility to perform near-edge X-ray absorption fine structure (NEXAFS) studies that give detailed chemical information about the surface species, and insight in their adsorption geometry. This method, together with HR-XPS, was used to study the surface reaction of the heteroatom-free LOHC system dicyclohexylmethane/diphenylmethane (DCHM/DPM) (see Chapter 4.5) on Pt(111). In addition, laboratory based temperature programmed desorption (TPD) measurements provided for complementary information about the desorbing molecules in the gas phase. The results show that dehydrogenation of cyclohexyl groups proceeds in steps by forming π-allylic intermediates. We find that DCHM dehydrogenates in the range of 200 - 260 K to form a double-sided π-allylic species coadsorbed with hydrogen. Between 260 and 330 K, ~30% of the surface species desorb, while for the other part one of the π-allyls reacts to a phenyl group between 260 and 330 K; this is accompanied by associative hydrogen desorption. Above 360 K, the other π-allyl dehydrogenates to a phenyl ring. This is accompanied by C-H bond scission at the methylene group, which is an unwanted decomposition step in the hydrogen storage cycle, as it alters the original hydrogen carrier DCHM. Above 450 K, further decomposition steps occur that are assigned to C-H abstraction at the phenyl rings.

In Chapter 5.1, fundamental studies on the formation of carbide-modified Mo(110) and Mo(100) single crystal surfaces have been performed. Molybdenum carbide is a possible candidate for replacing Pt-group-based dehydrogenation catalysts. On Mo(110), the preparation of monolayer

and bulk carbides was performed by exposure to ethylene at 1200 K and followed by continuously recording XP spectra. For the bulk carbide we find a surface coverage of 0.55 ± 0.06 ML. The result indicates a very similar surface structure compared to the C-terminated (001) surface of orthorhombic Mo_2C, where single carbon atoms are found in the three-fold hollow sites of the quasi-hexagonal Mo lattice. For the monolayer carbide on Mo(110), we find a coverage of 0.43 ± 0.06 ML. Together with density functional theory (DFT) calculations, a (4×4) surface structure is proposed, where carbon atoms form dimers in the nearest neighbor three-fold hollow sites. On Mo(100), a well-defined monolayer carbide with a coverage of 0.95 ± 0.10 ML was prepared at 1200 K. DFT calculations show that carbon occupies the four-fold hollow sites of the (100)-facet, which is in excellent agreement with the (1×1) pattern found in LEED. A bulk carbide on Mo(100) was prepared by exposure to ethylene at 900 K followed by flashes to 1300 K. This preparation method most likely leads to faceting of the surface. For both the Mo(110) and the Mo(100) surfaces, carbide removal by exposure to oxygen was investigated.

To study the difference in reactivity between the monolayer and bulk carbide on Mo(110), carbon monoxide (CO) adsorption and heating experiments were performed on both surfaces. At 140 K, on the monolayer carbide two molecular adsorption species are found, and the total coverage of molecular CO is ~0.7 ML, while a fraction of CO dissociates (~0.05 ML) during adsorption. The bulk carbide shows a similar behavior: three molecular adsorption species are found, yielding a total coverage of molecular CO of ~0.6 ML, while ~0.1 ML of CO adsorb dissociatively. Upon heating, on the monolayer carbide in the range of 250 to 400 K most of the molecular CO desorbs (~75%, ~0.55 ML), while the other part dissociates (~25%, ~0.15 ML). On the bulk carbide in the range of 300-460 K, ~85% desorb (0.5 ML) and ~15% (0.1 ML) dissociate. Up to 800 K, for both the monolayer and bulk carbide the surface is only covered by the products of dissociation, atomic carbon and oxygen. In the range of 800 to 1050 K, a decrease of the adsorbed oxygen and carbon species is observed due to associative desorption of CO, leading to the “clean” carbide surfaces as prepared before adsorption. In conclusion, the reactivity of both surfaces is quite similar. These studies provide for the basic knowledge needed for future experiments with LOHCs on molybdenum carbide.

7 Zusammenfassung

Um die heutzutage hauptsächlich genutzten fossilen Brennstoffe durch erneuerbare Energiequellen zu ersetzen, müssen effiziente Speichertechnologien entwickelt werden. Einerseits schwankt die Verfügbarkeit von Energie aus Windkraftwerken und Photovoltaik durch den Tag-Nacht-Zyklus und wird vom Wetter beeinflusst, andererseits hängt der Energieverbrauch von der Tages- und Jahreszeit ab. Unter den potentiellen Energiespeichern weist Wasserstoff die höchste gravimetrische Speicherdichte auf (33 kWh pro kg H_2), allerdings erfordern physikalische Speichermethoden hohe Drücke oder sehr niedrige Temperaturen. Diese Speichertechnologien sind nicht ungefährlich und benötigen eine erhebliche Menge an Energie zur Verflüssigung oder Kompression. Zudem treten bei längerer Speicherung Verluste durch Verdampfung bei Verflüssigung sowie durch Diffusion bei Speicherung unter Druck auf.

Eine mögliche Alternative zu diesen physikalischen Speichermethoden ist die chemische Speicherung von Wasserstoff durch Hydrierung von flüssigen organischen Wasserstoffträgern (engl. liquid organic hydrogen carrier, LOHC). Dabei handelt es sich um organische Moleküle, die bei Umgebungstemperatur flüssig sind und ähnliche physikalische und chemische Eigenschaften wie Diesel aufweisen. Das Konzept sieht die Gewinnung des Wasserstoffs an einem energiereichen Ort vor, z.B. durch Elektrolyse von Wasser aus Strom aus einer Windkraftanlage; die LOHCs werden mit dem gewonnenen Wasserstoff hydriert und werden so zur energiereichen Substanz. Die Eigenschaften der Flüssigkeit erlauben es, diese relativ einfach und kostengünstig an den Ort des Energiemangels zu bringen, z.B. durch Nutzung von vorhandener Infrastruktur für die Speicherung und Verteilung von flüssigen Energieträgern (Öltanker, Tankwagen, Tankstellen…). Die Dehydrierung und die Konsumierung der Energie erfolgt am Ort des Energiemangels. Anschließend sorgt der Rücktransport der energiearmen Substanz zum Ort der Energiegewinnung für den Abschluss eines Zyklus der Speichertechnologie. Hierbei erfolgen die chemischen Reaktionen sowohl der Hydrierung als auch der Dehydrierung in Reaktoren mittels Katalysatoren die Platin-ähnliche Metalle enthalten.

Untersuchungen im Bereich der Oberflächenchemie tragen zum grundlegenden Verständnis von heterogener Katalyse an Oberflächen bei. In dieser Arbeit werden einige sehr aussagekräftige experimentelle Methoden (siehe Kapitel 3) zur Untersuchung der Dehydrierung und Zersetzung LOHCs auf atomar hochdefinierten, Pt(111)- und Pd(111)- Einkristallen im Ultrahochvakuum (UHV) verwendet. Es wird gezeigt, dass sich Synchrotron-basierte spektroskopische Methoden exzellent dazu eignen, um chemische Reaktionen von großen organischen Molekülen auf Oberflächen zu untersuchen. Synchrotron-Lichtquellen der dritten Generation, wie der Berliner

Elektronenspeicherring für Synchrotronstrahlung (BESSY II) am Helmholtz-Zentrum Berlin (HZB), bieten Röntgenstrahlung hoher Intensität und geringer spektraler Linienbreite. Dies erlaubt es, schnelle Messungen mittels Photoelektronenspektroskopie, mit zugleich hoher spektraler Auflösung durchzuführen (engl. high-resolution X-ray photoelectron spectroscopy, HR-XPS). Mit dieser Methode lassen sich chemische Reaktionen nachverfolgen, die auf Zeitskalen im Bereich von Sekunden stattfinden. Das Verständnis dieser Modellsysteme auf molekularer Ebene bietet die Basis für eine wissensbasierte Entwicklung und Optimierung der Speichertechnologie.

Die Oberflächenreaktion des (vollhydrierten) LOHC-Moleküls Dodecahydro-N-ethylcarbazol (H_{12}-NEC) auf Pt(111) wurde mittels HR-XPS untersucht (siehe Kapitel 4.1 u. 4.2). Dazu wurde das Molekül zunächst bei 140 K auf der Pt-Oberfläche adsorbiert; anschließend erfolgte ein Heizexperiment bei einer Rate von 0.5 K/s. Der erste Reaktionsschritt beinhaltet die Desorption der physisorbierten Multilage bis ca. 240 K, wodurch nur die chemisorbierte Monolage von H_{12}-NEC auf der Oberfläche verbleibt. Ab Temperaturen über 200 K findet man die Dehydrierung der Kohlenstoffatome des Pyrrolidinrings; das resultierende H_8-NEC stellt das erste stabile Zwischenprodukt bei ~330 K auf der Oberfläche dar. Im nächsten Schritt dehydriert diese Spezies weiter an den äußeren Kohlenstoffringen bis 380 K. Oberhalb von 390 K findet man die unerwünschte Dealkylierungs-Reaktion von NEC. Das resultierende Carbazol ist ein unerwünschtes Reaktionsprodukt, da es den Schmelzpunkt des LOHC-Gemisches erhöht und somit die weitere Verwendung als Energiespeicher erschwert. Bei 450 K ist Carbazol die dominante Oberflächenspezies und bei noch höheren Temperaturen findet eine weitere Zersetzung des Moleküls auf der Katalysatoroberfläche statt. Die Ergebnisse dieser Untersuchung zeigen, dass N-Ethylcarbazol in einem bestimmten Temperaturbereich als regenerierbarer Wasserstoffspeicher genutzt werden kann, wobei 380 K die ideale Temperatur zur Dehydrierung unter Ultrahochvakuum-Bedingungen darstellt.

Um den Einfluss der Alkylkette auf die Oberflächenreaktion zu verstehen, wurden zusätzlich die NEC-Derivate Dodecahydro-N-propylcarbazol (H_{12}-NPC) und Dodecahydro-N-butylcarbazol (H_{12}-NBC) auf Pt(111) untersucht (siehe Kapitel 4.3). Die Reaktion folgt den selben Schritten wie die von H_{12}-NEC und die Stabilität der Moleküle ist ebenfalls ähnlich, da für alle drei Fälle die Dealkylierung bei etwa 380-390 K startet. Es lässt sich jedoch eine Abnahme der Reaktivität mit der Alkylkettenlänge feststellen: bei 450 K zeigt NEC eine Umwandlung zu Carbazol von ca. 70%, NPC allerdings nur eine von ~40% und NBC eine von ~20%. Bei 500 K ist kein klarer Trend mehr erkennen. Abschließend lässt sich sagen, dass sowohl Dehydrierung als auch Dealkylierung von der Länge der Alkylkette nur wenig bis gar nicht beeinflusst wird.

Um die Ergebnisse auf Pt(111) mit denen auf anderen Materialien zu vergleichen, wurde die Stabilität von H_{12}-NEC auf Pd(111) untersucht (siehe Kapitel 4.4). Die HR-XPS-Ergebnisse zeigen, dass auf Pd(111) die Dealkylierung bereits bei etwa 360 K startet und somit um 30 K niedriger als auf Pt(111). Dies ist ein Hinweis auf eine niedrigere Aktivierungsenergie auf Pd(111) im Vergleich zu Pt(111) und könnte zur früheren Inaktivierung dieses Katalysators durch Kohlenstoffablagerungen auf der Oberfläche führen.

Synchrotron-Lichtquellen lassen eine Variation der Photonenenergie zu. Dies bietet die Möglichkeit, Röntgenabsorptionsmessungen in Abhängigkeit der Anregungsenergie durchzuführen. Die sogenannte Nahkanten-Röntgenabsorptionsspektroskopie (engl. Near-Edge X-ray Absorption Fine Structure, NEXAFS) liefert detaillierte chemische Information über die Oberflächenspezies und lässt Schlüsse auf die Absorptionsgeometrie zu. Zusammen mit HR-XPS wurde diese Methode verwendet, um die Oberflächenreaktion der LOHC-Moleküle Dicyclohexylmethan (DCHM) und Diphenylmethan (DPM) auf Pt(111) zu untersuchen (siehe Kapitel 4.5). Die Ergebnisse zeigen, dass die Dehydrierung der Cyclohexyl-Gruppen in Schritten stattfindet. Zunächst bildet sich im Bereich von 200 bis 260 K eine doppelseitige π-Allyl-Spezies, die durch eine intakte Methylenbrücke verbunden ist. Im nächsten Schritt (260 bis 330 K) desorbieren etwa 30% der Moleküle, während der andere Teil zu einer einseitigen π-Allyl-Spezies dehydriert, bestehend aus dem π-Allyl auf der einen und einer Phenylgruppe auf der anderen Seite. Oberhalb von 360 K dehydriert das verbleibende π-Allyl zu einer Phenylgruppe; im gleichen Schritt kommt es auch zum Verlust von einem der Wasserstoffatome an der Methylenbrücke. Die letzte Reaktion und die folgende Dehydrierung der Phenylringe oberhalb von 450 K führen zu Kohlenstoffablagerungen auf der Oberfläche unter UHV-Bedingungen.

Kapitel 5.1 beinhaltet grundlegende Untersuchungen der Bildung von Carbid-modifizierten Molybdän (110) und (100) Einkristallen. Molybdäncarbid ist ein möglicher Kandidat für den Ersatz von Platin-basierten Katalysatoren für Dehydrierungsreaktionen durch kostengünstigere Materialien. Auf Mo(110) wurden Monolagen- und Volumencarbide hergestellt, in dem die Probe bei 1200 K Ethylengas ausgesetzt wurde. Die Bildung der Carbidschichten wurde dabei mittels HR-XPS verfolgt. Das Volumencarbid hat eine Oberflächen-Bedeckung durch Kohlenstoff von 0.55 ± 0.06 ML; die Oberflächenstruktur weist Ähnlichkeiten mit der Kohlenstoff-terminierten (001)-Oberfläche von orthorhombischem Mo_2C auf, bei der Kohlenstoffatome die dreifach koordinierten Adsorptionsplätze besetzen. Für das Monolagencarbid wurde eine Bedeckung von 0.43 ± 0.06 ML bestimmt. Zusammen mit Berechnungen mittels Dichtefunktionaltheorie (DFT) wurde eine (4×4)-Struktur der Oberflächeneinheitszelle vorgeschlagen, wo Kohlenstoffatome

Dimere in den langgezogenen dreifach-koordinierten Adsorptionsplätzen bilden. Auf Mo(100) wurde nach der gleichen Methode ein Monolagencarbid mit einer Bedeckung von 0.95 ± 0.10 ML bei 1200 K hergestellt. Kohlenstoff besetzt hier die vierfach-koordinierten Adsorptionsplätze. Ein Volumencarbid wurde auf Mo(100) ebenfalls erzeugt; dafür wurde die Probe bei 900 K Ethylengas ausgesetzt, gefolgt durch kurzes Anlassen auf 1300 K. Diese Methode führt jedoch höchstwahrscheinlich zur Facettierung der Oberfläche. Für beide Einkristall-Oberflächen wurde auch die Entfernung des Carbids von der Oberfläche durch Sauerstoffdosierung untersucht.

Um die Unterschiede in der Reaktivität von Monolagen und Volumencarbid auf Mo(110) zu untersuchen, wurden Adsorptions- und Heizexperimente von Kohlenmonoxid (CO) auf beiden Oberflächen durchgeführt. Bei 140 K finden sich auf dem Monolagencarbid zwei Adsorptionsplätze; die Gesamtbedeckung von CO beträgt ~0.7 ML, wobei ein Teil des CO während der Adsorption dissoziiert (~0.05 ML). Das Volumencarbid zeigt eine ähnliche Verhaltensweise: es finden sich drei verschiedene molekular adsorbierte Spezies; die Gesamtbedeckung beträgt ~0.6 ML, wobei ebenfalls ein Teil (~0.15 ML) dissoziiert. Während des Heizens der Probe desorbieren im Falle des Monolagencarbids zwischen 250 und 400 K etwa 75% des CO, wobei der andere Teil dissoziiert (~25%). Beim Volumencarbid desorbieren in etwa ~85% des CO zwischen 300 und 460 K, während der Rest (~15%) dissoziiert. Bis ca. 800 K finden sich auf beiden Oberflächen nur die Produkte der Dissoziation (adsorbierter atomarer Kohlenstoff und Sauerstoff). Im Bereich von 800 bis 1050 K desorbieren diese beiden Adsorbate assoziativ, d.h. durch Bildung von CO, von beiden Oberflächen. Dies führt zurück zum Ausgangszustand vor den Adsorptionsexperimenten. Diese Untersuchungen liefern die Grundlage für zukünftige Experimente mit LOHCs auf Molybdäncarbid.

8 Danksagungen

Zunächst möchte ich mich recht herzlich bei Prof. Hans-Peter Steinrück für die hervorragende Betreuung bedanken. Jegliche Diskussionen gestalteten sich stets konstruktiv, ermutigend und motivierend, sodass dies maßgeblich zum Erfolg meiner Promotion in Erlangen beigetragen hat.

Besonderer Dank für die Betreuung meines Promotionsthemas gilt Dr. Christian Papp, Leiter der Synchrotron-Gruppe, der immer ein offenes Ohr für Ideen hatte und der wesentlich zum zeitnahen Abschluss meines Promotionsvorhabens beitrug.

In der Synchrotrongruppe werden die meisten Messungen nicht im Labor in Erlangen, sondern im Schichtbetrieb am Synchrotron in Berlin durchgeführt. Hier war Teamwork gefragt, daher möchte ich allen Kollegen danken, die mich in der Zeit in Berlin unterstützt hatten: Dr. Oliver Höfert, Max Amende, Dr. Stefan Schernich, Karin Gotterbarm, Udo Bauer, Florian Späth, Dr. Wei Zhao, Carina Bronnbauer, Claudia Wöckel, Tao Xu sowie Susanne Mohr.

Im Rahmen meiner Promotion wurden unter meiner Anleitung vier Bachelorarbeiten und eine Masterarbeit angefertigt. Die Ergebnisse von Udo Bauer (Masterarbeit) sowie Philipp Bachmann sowie Fabian Düll (Bachelorarbeiten) trugen teilweise zu dieser Arbeit bei, wobei ich mich für die gute Arbeit bedanken möchte.

Die LOHCs wurden von der Gruppe von Prof. Peter Wasserscheid (Nicole Brückner, Marcus Koch) zur Verfügung gestellt. Dichtefunktionaltheorie-Rechnungen für Molybdäncarbid wurden in der Gruppe von Prof. Andreas Görling (Dr. Christian Neiss, Sven Maisel) durchgeführt. Ich danke für die äußerst fruchtbare Kooperation mit beiden Gruppen.

Zur Durchführung der Messungen braucht man funktionierende Ausrüstung. Die Hilfe von Herrn Bernd Kress (technische Unterstützung) und Hans-Peter Bäumler (Elektroniker, Bau der Hochspannungsbox für NEXAFS-Messungen) war für die erfolgreiche Durchführung der Messzeiten unbedingt nötig. Des Weiteren danke ich der gesamten Mechanikwerkstatt und dem Leiter derselben, Friedhold Wölfel, für die zeitnahe Erledigung jeglicher Reparaturen und für die höchst präzise ausgeführten Spezialanfertigungen. Ohne Stefan Cramm vom FZ Jülich wäre das NEXAFS-Setup mit Sicherheit nicht so schnell einsatzbereit gewesen; ich danke ihm für die stundenlangen Diskussionen am BESSY und die technische Unterstützung.

Abschließend möchte ich meiner Familie für die Unterstützung und Geduld in 22 Jahren schulischer sowie akademischer Ausbildung bedanken.

9 Literature

1. British Petroleum Co., *BP Statistical Review of World Energy 2014*, Report 63, London, 2014.
2. D. Teichmann, W. Arlt, P. Wasserscheid and R. Freymann, *Energy Environ. Sci.*, 2011, **4**, 2767-2773.
3. A. Sartbaeva, V. L. Kuznetsov, S. A. Wells and P. P. Edwards, *Energy Environ. Sci.*, 2008, **1**, 79-85.
4. P. J. Hall, *Energ Policy*, 2008, **36**, 4363-4367.
5. B. Dunn, H. Kamath and J.-M. Tarascon, *Science*, 2011, **334**, 928-935.
6. The Electric Power Research Institute, *Electric Energy Storage Technology Options: A Primer on Applications, Costs & Benefits - An EPRI Executive Summary*, Report 1022261, 2010.
7. U. Eberle, M. Felderhoff and F. Schüth, *Angew. Chem. Int. Ed.*, 2009, **48**, 6608.
8. B. Sakintuna, F. Lamari-Darkrim and M. Hirscher, *Int. J. Hydrogen Energy*, 2007, **32**, 1121-1140.
9. G. A. Olah, *Angew. Chem. Int. Ed.*, 2005, **44**, 2636-2639.
10. K. Mazloomi and C. Gomes, *Renew. Sust. Energy Rev.*, 2012, **16**, 3024-3033.
11. G. Cipriani, V. Di Dio, F. Genduso, D. La Cascia, R. Liga, R. Miceli and G. Ricco Galluzzo, *Int. J. Hydrogen Energy*, 2014, **39**, 8482-8494.
12. R. H. Crabtree, *Energy Environ. Sci.*, 2008, **1**, 134-138.
13. G. W. H. Scherer and E. Newson, *Int. J. Hydrogen Storage*, 1998, **23**, 19-25.
14. D. Teichmann, W. Arlt and P. Wasserscheid, *Int. J. Hydrogen Energy*, 2012, **37**, 18118.
15. N. Brückner, K. Obesser, A. Bösmann, D. Teichmann, W. Arlt, J. Dungs and P. Wasserscheid, *ChemSusChem*, 2014, **7**, 229-235.
16. D. Teichmann, K. Stark, K. Muller, G. Zottl, P. Wasserscheid and W. Arlt, *Energy Environ. Sci.*, 2012, **5**, 9044-9054.
17. G. W. H. Scherer, PhD Thesis, ETH Zurich, 1997.
18. M. Markiewicz, Y. Q. Zhang, A. Bosmann, N. Bruckner, J. Thoming, P. Wasserscheid and S. Stolte, *Energy Environ. Sci.*, 2015, **8**, 1035-1045.
19. C. Gleichweit, M. Amende, U. Bauer, S. Schernich, O. Höfert, M. P. A. Lorenz, W. Zhao, M. Müller, M. Koch, P. Bachmann, P. Wasserscheid, J. Libuda, H.-P. Steinrück and C. Papp, *J. Chem. Phys.*, 2014, **140**.
20. IUPAC, *Compendium of Chemical Terminology, 2nd ed. (the "Gold Book")*, Blackwell Scientific Publications, Oxford, 1997.
21. J. E. House, *Principles of Chemical Kinetics*, Academic Press, London, 2007.
22. K. W. Kolasinski, *Surface Science: Foundations of Catalysis and Nanoscience*, John Wiley & Sons, Chichester, 2012.
23. J. H. Larsen and I. Chorkendorff, *Surf. Sci. Rep.*, 1999, **35**, 163-222.
24. S. K. Eriksson, M. Hahlin, J. M. Kahk, I. J. Villar-Garcia, M. J. Webb, H. Grennberg, R. Yakimova, H. Rensmo, K. Edström, A. Hagfeldt, H. Siegbahn, M. O. M. Edwards, P. G. Karlsson, K. Backlund, J. Åhlund and D. J. Payne, *Rev. Sci. Instrum.* , 2014, **85**, 075119.
25. M. Salmeron and R. Schlögl, *Surf. Sci. Rep.*, 2008, **63**, 169-199.
26. B. Hammer and J. K. Nørskov, *Surf. Sci.*, 1995, **343**, 211-220.
27. B. Hammer and J. K. Nørskov, in *Adv. Catal.*, ed. H. K. Bruce C. Gates, Academic Press, 2000, vol. Volume 45, pp. 71-129.
28. H. Wern, R. Courths, G. Leschik and S. Hüfner, *Z. Phys. B. Con. Mat.*, 1985, **60**, 293-310.

29. D. McDonald and L. B. Hunt, *A history of platinum and its allied metals*, Europa Publications Ltd, London, 1982.
30. R. E. Krebs, *The History and Use of Our Earth's Chemical Elements: A Reference Guide, Second Edition*, Greenwood Press, Westport, 2006.
31. N. M. Marković and P. N. Ross Jr, *Surf. Sci. Rep.*, 2002, **45**, 117-229.
32. M. Sobota, I. Nikiforidis, M. Amende, B. S. Zanón, T. Staudt, O. Höfert, Y. Lykhach, C. Papp, W. Hieringer, M. Laurin, D. Assenbaum, P. Wasserscheid, H.-P. Steinrück, A. Görling and J. Libuda, *Chem. Eur. J.*, 2011, **17**, 11542-11552.
33. C.-J. Yang, *Energ Policy*, 2009, **37**, 1805-1808.
34. R. B. Levy and M. Boudart, *Science*, 1973, **181**, 547-549.
35. H. H. Hwu and J. G. Chen, *Chem. Rev.*, 2005, **105**, 185-212.
36. P. Willmott, *An Introduction to Synchrotron Radiation: Techniques and Applications*, John Wiley & Sons, Chichester, 2011.
37. B. Povh, K. Rith, C. Scholz, F. Zetsche and W. Rodejohann, *Teilchen und Kerne: Eine Einführung in die physikalischen Konzepte*, Springer Spektrum, Berlin, 2014.
38. G. Hähner, *Chem. Soc. Rev.*, 2006, **35**, 1244-1255.
39. A. Einstein, *Annalen der Physik*, 1905, **322**, 132-148.
40. S. Suga and A. Sekiyama, *Photoelectron Spectroscopy*, Springer, Heidelberg, 2014.
41. C. Papp and H.-P. Steinrück, *Surf. Sci. Rep.*, 2013, **68**, 446–487.
42. K. Siegbahn, C. Nordling, A. Fahlman, H. Nordberg, K. Hamrin, J. Hedman, G. Johannson, T. Bergmark, S. E. Karlsson, J. Lindgren and B. Lindberg, *Electron Spectroscopy for Chemical Analysis; Atomic, Molecular and Solid State Structure Studies by means of Electron Spectroscopy*, Almquist and Wiksells, Stockholm, 1967.
43. M. P. Seah and W. A. Dench, *Surf. Interface Anal.*, 1979, **1**, 2-11.
44. S. Hüfner, *Photoelectron Spectroscopy: Principles and Applications*, Springer, Heidelberg, 1996.
45. J. G. Choi and L. T. Thompson, *App. Surf. Sci.*, 1996, **93**, 143-149.
46. R. Denecke and N. Martensson, in *Adsorbed Layers on Surfaces*, ed. H. P. Bonzel, Springer, Berlin, 2005, vol. 42A4, ch. 15, pp. 388-421.
47. D. P. Woodruff and A. M. Bradshaw, *Rep. Prog. Phys.*, 1994, **57**, 1029-1080.
48. M. Kinne, PhD Thesis, Universtität Erlangen-Nürnberg, 2004.
49. J. Stöhr, *NEXAFS Spectroscopy*, Springer, Berlin, 1992.
50. J. L. Solomon, R. J. Madix and J. Stöhr, *Surf. Sci.*, 1991, **255**, 12-30.
51. R. Püttner, C. Kolczewski, M. Martins, A. S. Schlachter, G. Snell, M. Sant'Anna, J. Viefhaus, K. Hermann and G. Kaindl, *Chem. Phys. Lett.*, 2004, **393**, 361-366.
52. J. Gross, *Massenspektrometrie - Ein Lehrbuch*, Springer, Heidelberg, 2013.
53. J. W. Niemantsverdriet, *Spectroscopy in Catalysis*, Wiley-VHC, Hoboken, 2007.
54. A. M. de Jong and J. W. Niemantsverdriet, *Surf. Sci.*, 1990, **233**, 355-365.
55. E. Habenschaden and J. Küppers, *Surf. Sci. Lett.*, 1984, **138**, L147-L150.
56. P. A. Redhead, *Vacuum*, 1962, **12**, 203-211.
57. R. Denecke, M. Kinne, C. M. Whelan and H.-P. Steinrück, *Surf. Rev. Lett.*, 2002, **9**, 797.
58. G. Scoles, *Atomic and Molecular Beam Methods*, Oxford University Press, New York, 1988.
59. G. Held, S. Uremović, C. Stellwag and D. Menzel, *Rev. Sci. Instrum.* , 1996, **67**, 378-383.
60. W. Braun, H. P. Steinrück and G. Held, *Surf. Sci.*, 2005, **574**, 193-204.
61. P. Feulner and D. Menzel, *J. Vac. Sci. Technol.*, 1980, **17**, 662-663.
62. E. Newson, T. Haueter, P. Hottinger, F. Von Roth, G. W. H. Scherer and T. H. Schucan, *Int. J. Hydrogen Energy*, 1998, **23**, 905-909.

63. R. B. Biniwale, S. Rayalu, S. Devotta and M. Ichikawa, *Int. J. Hydrogen Energy*, 2008, **33**, 360-365.
64. G. W. H. Scherer, E. Newson and A. Wokaun, *Int. J. Hydrogen Energy*, 1999, **24**, 1157-1169.
65. F. Sotoodeh, PhD Thesis, The University of British Columbia, 2011.
66. K. M. Eblagon, K. Tam, K. M. K. Yu and S. C. E. Tsang, *J. Phys. Chem. C*, 2012, **116**, 7421-7429.
67. F. Sotoodeh, L. Zhao and K. J. Smith, *Appl. Catal. A-Gen.*, 2009, **362**, 155-162.
68. F. Sotoodeh and K. J. Smith, *J. Phys. Chem. C*, 2013, **117**, 194.
69. K. Müller, J. Völkl and W. Arlt, *Energy Technol.*, 2013, **1**, 20-24.
70. M. Zenner, D. Teichmann, M. Pierro and J. Dungs, *ATZ*, 2012, 940-947.
71. M. Amende, C. Gleichweit, K. Werner, S. Schernich, W. Zhao, M. P. A. Lorenz, O. Höfert, C. Papp, M. Koch, P. Wasserscheid, M. Laurin, H.-P. Steinrück and J. Libuda, *ACS Catal.*, 2014, **4**, 657-665.
72. C. Gleichweit, M. Amende, S. Schernich, W. Zhao, M. P. A. Lorenz, O. Höfert, N. Brückner, P. Wasserscheid, J. Libuda, H.-P. Steinrück and C. Papp, *ChemSusChem*, 2013, **6**, 974-977.
73. F. Sotoodeh, B. J. M. Huber and K. J. Smith, *Appl. Catal. A-Gen.*, 2012, **419-420**, 67-72.
74. Z. Wang, I. Tonks, J. Belli and C. M. Jensen, *J. Organomet. Chem.* , 2009, **694**, 2854-2857.
75. C. Papp, P. Wasserscheid, J. Libuda and H.-P. Steinrück, *Chem. Rec.*, 2014, **14**, 879-896.
76. S. Haq and D. A. King, *J. Phys. Chem.*, 1996, **100**, 16957-16965.
77. K. M. Eblagon, D. Rentsch, O. Friedrichs, A. Remhof, A. Zuettel, A. J. Ramirez-Cuesta and S. C. Tsang, *Int. J. Hydrogen Energy*, 2010, **35**, 11609-11621.
78. K. M. Eblagon, K. Tam, K. M. K. Yu, S.-L. Zhao, X.-Q. Gong, H. He, L. Ye, L.-C. Wang, A. J. Ramirez-Cuesta and S. C. E. Tsang, *J. Phys. Chem. C*, 2010, **114**, 9720.
79. M. Yang, Y. Dong, S. Fei, Q. Pan, G. Ni, C. Han, H. Ke, Q. Fang and H. Cheng, *RSC Adv.*, 2013, **3**, 24877-24881.
80. F. Sotoodeh and K. J. Smith, *J. Catal.*, 2011, **279**, 36-47.
81. M. Amende, S. Schernich, M. Sobota, I. Nikiforidis, W. Hieringer, D. Assenbaum, C. Gleichweit, H.-J. Drescher, C. Papp, H.-P. Steinrück, A. Görling, P. Wasserscheid, M. Laurin and J. Libuda, *Chem. Eur. J.*, 2013, **19**, 10854-10865.
82. A. P. Hitchcock, D. C. Newbury, I. Ishii, J. Stöhr, J. A. Horsley, R. D. Redwing, A. L. Johnson and F. Sette, *J. Chem. Phys.* , 1986, **85**, 4849-4862.
83. A. L. Johnson, E. L. Muetterties and J. Stöhr, *JACS*, 1983, **105**, 7183-7185.
84. S. T. Oyama, *The chemistry of transition metal carbides and nitrides*, Blackie A&P, Glasgow, 1996.
85. L. I. Johansson, *Surf. Sci. Rep.*, 1995, **21**, 179-250.
86. J. G. Chen, *Chem. Rev.*, 1996, **96**, 1477-1498.
87. W. F. Chen, J. T. Muckerman and E. Fujita, *Chem. Commun.*, 2013, **49**, 8896-8909.
88. A. L. Stottlemyer, T. G. Kelly, Q. Meng and J. G. Chen, *Surf. Sci. Rep.*, 2012, **67**, 201-232.
89. M. Bode, R. Pascal and R. Wiesendanger, *Surf. Sci.*, 1995, **344**, 185-191.
90. P. F. Lyman and D. R. Mullins, *Phys. Rev. B*, 1995, **51**, 13623-13630.
91. T. Schöberl, *Surf. Sci.*, 1995, **327**, 285.
92. L. Ovari, J. Kiss, A. P. Farkas and F. Solymosi, *Surf. Sci.*, 2004, **566**, 1082-1086.
93. M. B. Young and A. J. Slavin, *Surf. Sci.*, 1991, **245**, 56-64.
94. B. Frühberger and J. G. Chen, *Surf. Sci.*, 1995, **342**, 38-46.
95. C. Guillot, R. Riwan and J. Lecante, *Surf. Sci.*, 1976, **59**, 581-592.

96. A. C. Lausche, J. A. Schaidle and L. T. Thompson, *Appl. Catal. A-Gen.*, 2011, **401**, 29-36.
97. M. Kottcke, R. Döll, W. Weiß, F. Seiferlein, W. Arabczyk, L. Hammer and K. Heinz, *Surf. Sci.*, 1996, **352-354**, 592-596.
98. S. H. Overbury and P. C. Stair, *J. Vac. Sci. Technol. A.*, 1983, **1**, 1055-1058.
99. M. Smedh, S. F. Diaz and C. T. Campbell, *Phys. Rev. B*, 2003, **67**, 2054011-2054018.
100. J. R. Kitchin, PhD Thesis, University of Delaware, 2004.
101. B. Frühberger, J. G. Chen, J. Eng and B. E. Bent, *J. Vac. Sci. Technol. A.*, 1996, **14**, 1475-1481.
102. R. L. Lo, K. I. Fukui, S. Otani, S. T. Oyama and Y. Iwasawa, *Jpn. J. Appl. Phys. 1*, 1999, **38**, 3813-3815.
103. T. P. St. Clair, S. T. Oyama, D. F. Cox, S. Otani, Y. Ishizawa, R. L. Lo, K. I. Fukui and Y. Iwasawa, *Surf. Sci.*, 1999, **426**, 187-198.
104. A. J. Jaworowski, M. Smedh, M. Borg, A. Sandell, A. Beutler, S. L. Sorensen, E. Lundgren and J. N. Andersen, *Surf. Sci.*, 2001, **492**, 185-194.

A. Appendix [P1-P7]

[P1] *Dehydrogenation of Dodecahydro-N-ethylcarbazole on Pt(111)*
C. Gleichweit, M. Amende, S. Schernich, W. Zhao, M.P.A. Lorenz, O. Höfert, N. Brückner, P. Wasserscheid, J. Libuda and H.-P. Steinrück
ChemSusChem, 2013, **6**, 974-977

[P2] *Model Catalytic Studies of Liquid Organic Hydrogen Carriers: Dehydrogenation and Decomposition Mechanisms of Dodecahydro-N-ethylcarbazole on Pt(111)*
M. Amende, **C. Gleichweit**, K. Werner, S. Schernich, W. Zhao, M.P.A. Lorenz, O. Höfert, C. Papp, M. Koch, P. Wasserscheid, M. Laurin, H.-P. Steinrück and J. Libuda
ACS Catalysis, 2014, **4**, 657-665

[P3] *Alkyl chain length-dependent surface reaction of dodecahydro- N -alkylcarbazoles on Pt model catalysts*
C. Gleichweit, M. Amende, U. Bauer, S. Schernich, O. Höfert, M.P.A. Lorenz, W. Zhao, M. Müller, M. Koch, P. Bachmann, P. Wasserscheid, J. Libuda, H.-P. Steinrück and C. Papp
Journal of Chemical Physics, 2014, **140**, 204711

[P4] *Dehydrogenation Mechanism of Liquid Organic Hydrogen Carriers: Dodecahydro-N-ethylcarbazole on Pd(111)*
M. Amende, S. Schernich, M. Sobota, I. Nikiforidis, W. Hieringer, D. Assenbaum,
C. Gleichweit, H.-J. Drescher, C. Papp, H.-P. Steinrück, A. Görling, P. Wasserscheid,
M. Laurin and J. Libuda
Chemistry - A European Journal, 2013, **19**, 10854-10865

[P5] *Surface Reactions of Dicyclohexylmethane on Pt(111)*
C. Gleichweit, M. Amende, O. Höfert, T. Xu, F. Späth, N. Brückner, P. Wasserscheid, J. Libuda, H.-P. Steinrück and C. Papp
The Journal of Physical Chemistry C, 2015, **119**, 20299-20311

[P6] *Comparative study of the carbide-modified surfaces C/Mo(110) and C/Mo(100) using high resolution X-ray photoelectron spectroscopy*
C. Gleichweit, C. Neiss, S. Maisel, U. Bauer, F. Späth, O. Höfert, F. Vollnhals, M. Drost, H. Marbach, A. Görling, H.-P. Steinrück and C. Papp
Physical Review B, 2015, **92**, 014114

[P7] *Surface reaction of CO on carbide-modified Mo(110)*
C. Gleichweit, C. Neiss, S. Maisel, U. Bauer, F. Späth, S. Mohr, O. Höfert, J. Libuda, A. Görling, H.-P. Steinrück and C. Papp
in preparation

B. Appendix: NEXAFS Detector Drawings and Operating Instructions

Fig. B1 shows the wiring diagram of the used 4716 Channeltron detector and the grids in front of it. Fig. B3 shows the blueprints of the custom-made stainless steel housing including the quadruple feedthrough. Table B2 shows the technical data of the channeltron.

There are four vacuum feed-throughs that need to be wired correctly. The first grid (from the left) acts as a shielding to leave the space in front of the detector free of any electric fields. Next there is the repulsion grid; PEY detection needs this to be at negative voltage (labelled "Gitt", Voltage V_3, channel 3-5 of "NHS 6 040x-K1").

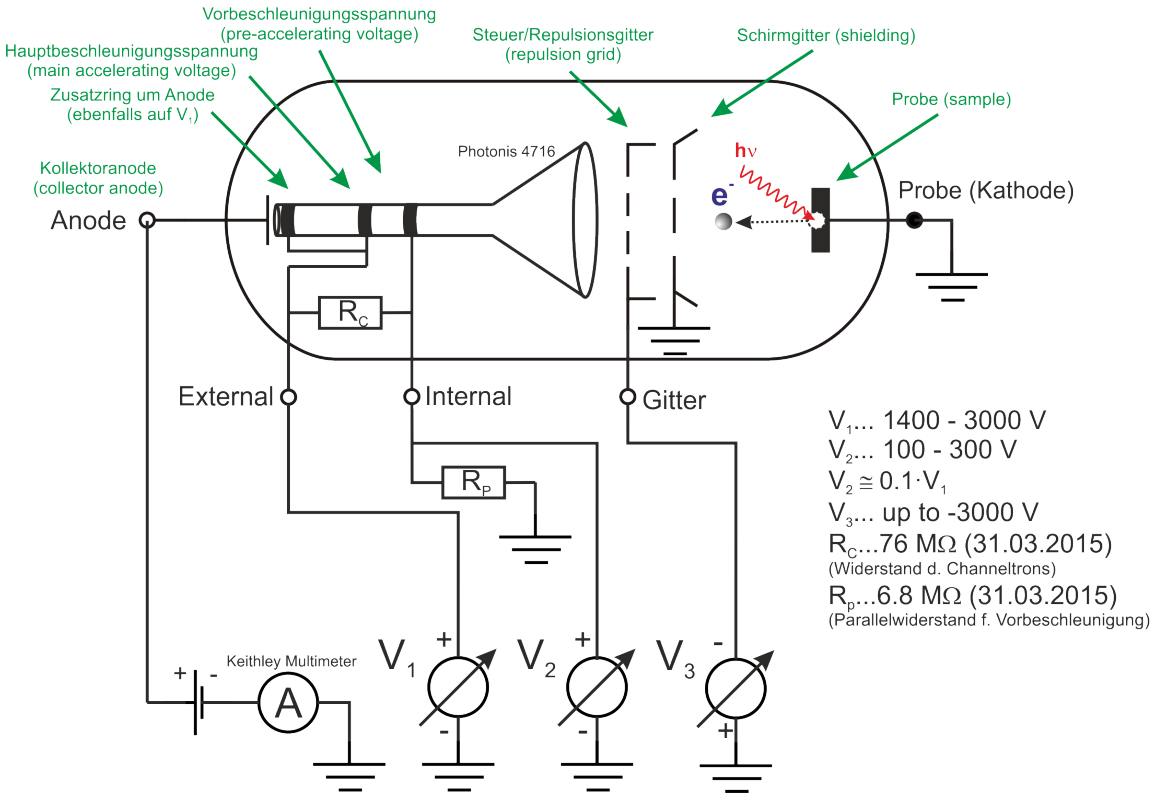

Fig. B1: *Wiring scheme of the partial electron yield (PEY) detector.*

If total electron yield (TEY) mode is applied, the grid needs to be at ground (simply disconnecting it will lead to charging!). Voltage V_1 is the main accelerating voltage that causes the signal gain and is labelled as "Ex" at the feedthrough. V_2 is a pre-accelerating voltage that takes the task of collecting all electrons that passed the repulsion grid and is labelled as "In" at the feedthrough. A typical choice would be 1/10 of V_1. The real operating voltage is then V_1 - V_2, because this is the voltage drop between front and back of the detector. V_1 and V_2 are both positive voltages for electron (and negative ion) detection (channel 0-2 of "NHS 6 040x-K1"). Note that the resistor R_p needs to be attached to the "In" connector in order for the voltage source to maintain a positive

current (otherwise it fails). Note that the detector can also be used to operate in positive ion detection mode.

The battery box, indicated at the wire of the collector anode in Fig. B1 needs to be handled with care. Fig. B2 shows a picture of the box including descriptions.

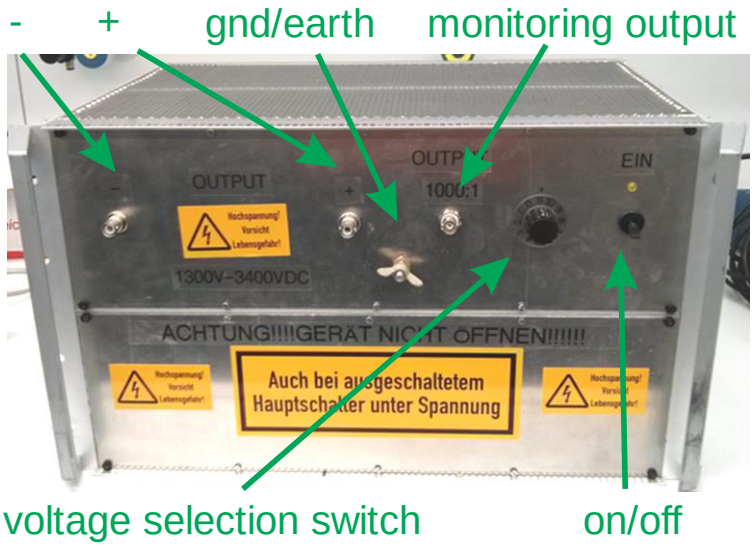

Fig. B2: Custom-built battery box

It has a rotary switch to select the voltage. There are three connectors at the front:

1. **"-" SHV connector:** It must be connected to the Keithley electrometer. For this an SHV to Triax cable connector is needed (typically SHV-BNC and BNC-Triax)
2. **"+" SHV connector:** This is the anode voltage (V_4) and needs to be connected directly to the UHV feedthrough (red cable).
3. **Monitoring output:** This is a voltage divider which enables the user to check the output voltage of the box. This only works if "-" is set to ground using an SHV ground connector and "+" is not connected. The multimeter can then be used to check the voltage (divided by 1000) using a BNC cable. The value is an additional value of 8% lower than displayed (because of technical reasons). See Table B1 for details.
4. **Ground/Earth:** The case of the battery box needs to be connected to the other electronic devices, as well as to the UHV setup directly. Not doing so might lead to charging/potential differences and thus to disturbed measurement signals.

Always turn off the box (switch to off) before changing the voltage stage. Not doing so might lead to a short circuit.
Any short circuit will result in loss of the fuse (as will confusing the – and + connector), which can only be replaced by an electronic engineer. Double check before turning the box on if everything is connected correctly. Never connect anything to "+" or "-" other than the intended devices.

Table B1: Battery box stages with voltage values (2015-04-01)

Switch position	$V_{monitor}$ [mV]	V_4 ("+") [V]
1	1350	1470
2	1663	1810
3	1976	2152
4	2132	2321
5	2289	2493
6	2444	2661
7	2601	2833
8	(defective)	(defective)
9	2758	3002
10	2924	3185
11	3090	3366

For a measuring signal to be obtained, the anode voltage V_4, chosen at the battery box, has to be always at higher voltage than the acceleration voltage V_1 ($V_4 > V_1 + 100$). The electrometer (typically Keithley) needs to be at the low voltage side, otherwise both battery box and electrometer will most probably be damaged.

The following procedure of operation is suggested:

1. Turn off any ion gauge, ion pump or filament in the analyzer chamber. The measured signal will be otherwise severely disturbed.
2. Turn on the electrometer to monitor the anode current while adjusting the voltages.
3. Raise the repulsion grid voltage to the desired value before (!!) any other voltage is applied (V_1,V_2,V_4=0). Raising any of the other voltages might result into damage if any electrons

are around the detector. If TEY mode is applied (V_3=0), be careful since the accelerating voltage might be much lower to reach the wanted bias.

4. Turn on the battery box (at stage 1) and wait for the electrometer to find a stable current readout. For this reason the "local" mode to display the value on the electrometer's screen has to be active, since otherwise the value is only displayed at the computer. A typical zero-current is 0.01-0.1 nA.
5. Switch on the X-ray light. Choose the X-ray energy which is expected to produce the most flux (e.g. 320 eV for the C 1*s* K-edge). The zero-current should not change much since no bias is expected at $V_1 = V_2 = 0$. Changing the slit while in operation might damage the detector, or lead to high currents that trigger the fuse of the battery box. The same is true for a change in sample orientation. Grazing incidence measurements produce a much higher signal.
6. Increase e.g. V_2 to 100-200 V.
7. Increase V_1 to ~1300 V. A signal should be obtained on the anode (electrometer). To increase this signal, the anode voltage V_4 and the acceleration voltage V_1 may be increased turn after turn in the following way:
    a. Turn off the battery box. Increase the voltage by one stage and turn it on again. Always turn off the battery box while switching to a higher stage!
    b. Increase V_1 to raise the gain as well while keeping $V_4 > V_1 + 100$ If the anode current starts dropping, this indicates that the voltages are too close together or even $V_1 > V_4$.
8. Start the measurement by ramping the photon energy.

In between or after the measurements, turn off the battery box and V_1. In any case, the simplest way to make sure the channeltron is safe is to turn off V_1, since this sets the gain to zero. The voltage source ("NHS 6 040x-K1") remembers the last used value and the Voltage can be retained easily by turning the channel on again.

If also the repulsion grid needs to be turned off, the other voltages have to be turned off before turning off the grid.

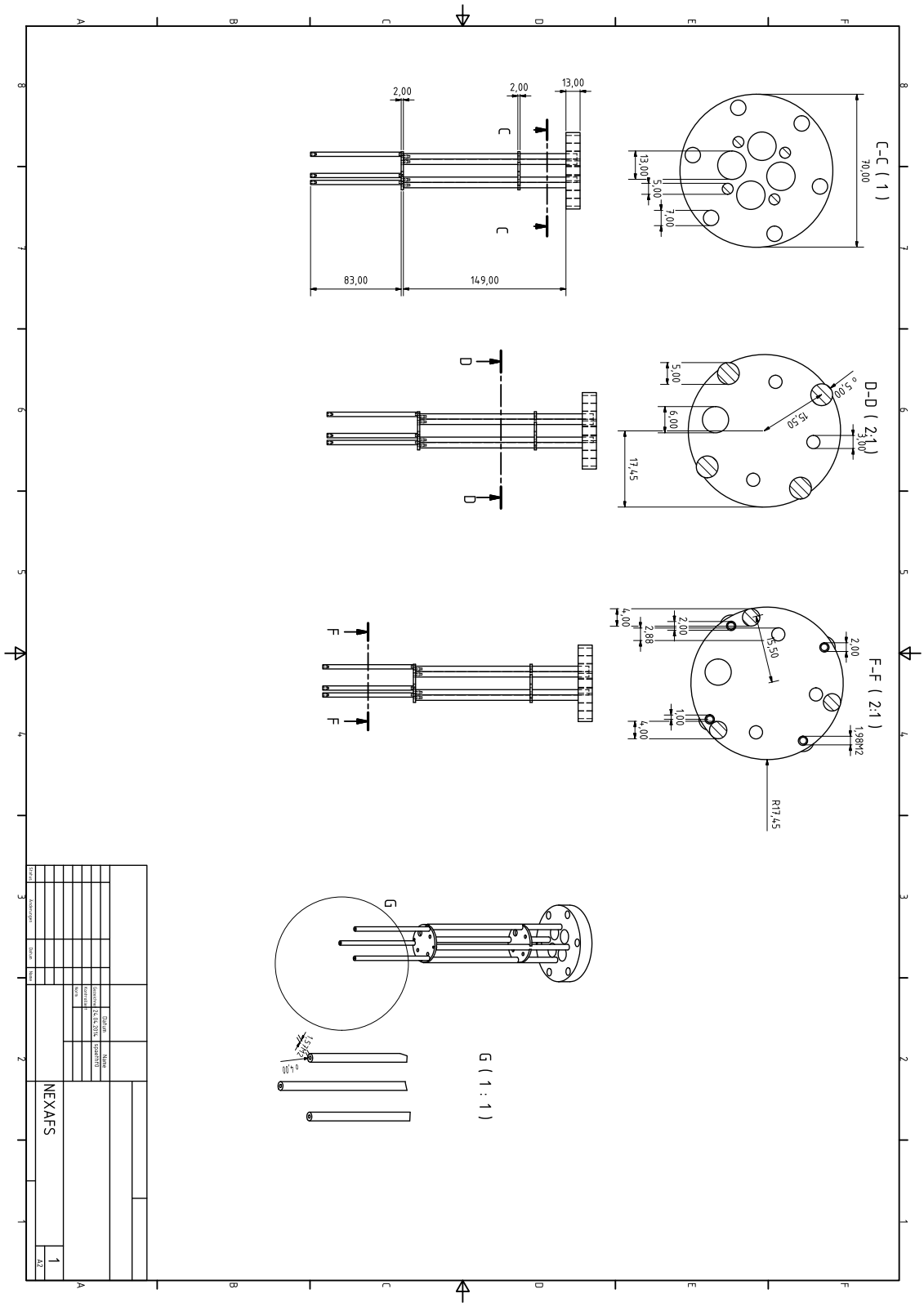

Fig. B3: Blueprint of the custom made stainless-steel device that houses the partial electron yield (PEY) detector

Table B2: Specifications of the 4716 Channeltron

Name	CEM 4716 TRI
Serial Number	CEM1Z4FB-1
Maximum Vacuum Bake Specification	8 Hours at 350˚C at 10^{-5} Torr
Operating Temperature Range:	-50˚ to 120˚C
Operation:	Analog
Maximum Operating Pressure:	5 x 10^{-6} Torr
Maximum Specified Operating Voltage:	3000 Volts (V_1-V_2)
Bias Current Range (3000 V):	35 to 55 Microamps
Resistance (31.03.2015):	76 MΩ
Maximum Dark Current:	1 x 10^{-11} A
Maximum Dark Count:	120 in 60 s
Maximum Linear Output Current:	10% of Bias Current (Typical)
Maximum Collector/Anode Current	1 μA (under operation stick to ~100 nA max)